X-ray and optical study of the 4U 1901+03

Foteini Mylonaki

Department of Physics

University of Crete, 2016

A thesis submitted for the degree of

Master of Science on Physics

Supervisors: Dr. Pablo Reig, Prof. Iossif Papadakis

Contents

Acknowledgments

Chapter 1

Introduction

1.1 X-ray Binary Systems

X-ray binaries are a class of binary stars that are luminous in X-rays. X-ray binaries are made up of a normal star called donor and a collapsed star called *accretor*, which is compact: a white dwarf, neutron star, or black hole. The compact object is usually surrounded by an accretion disc formed by the infalling flow of matter spiraling around it. The interaction between the accreted material and the huge gravitational field of the collapsed star produces an intense heating of the disc and makes it radiate in X-rays.

There three different major types of X-ray binaries depending on the type of the compact object: white dwarf X-ray binaries, neutron star X-ray binaries or black hole systems (see Fig. 1.1).

X-ray binaries with neutron stars and black holes can also be divided into low mass and high mass X-ray binaries, depending on the spectral type of the mass donor, as from this feature we can infer the manner in which the mass is transferred to the compact object and the environment surrounding the X-ray source.

1.2 Low mass X-ray binary.

An X-ray binary system in which the companion star has spectral type A or later, is known as low-mass X-ray binary. Accretion of material onto the compact object occurs via Roche-lobe overflow in the case of LMXBs. In this scenario the donor fills its Roche-lobe and material can overcome the gravitational pull of the donor star. As it spirals into the enormous gravitational well of the neutron star or black hole, the material is heated to millions of Kelvin giving rise to an X-ray emission.

1.3 High mass X-ray binary.

It is a binary star system that shows a hard X-ray spectrum because of the accretion of matter from the optical companion onto the neutron star. The stellar component in this system is a massive star: usually an O or B star, a Be star, or a blue supergiant. The X-ray emission from HMXBs is harder than that from LMXBs. In HMXBs, apart from the Roche-lobe overflow, accretion can occur via stellar winds from the donor which are captured by the compact object, as well as through circumstellar disc accretion in systems where the accretor passes through the disc at close approach resulting in transient X-ray outbursts (Waters& van Kerkwijk 1989, Reig 2011). According to the luminosity class of the optical star, we can subdivide HMXBs into Be/X-ray binaries (BeXB), when the optical star is a dwarf, subgiant or giant OBe star (luminosity class III, IV or V) and supergiant X-ray binaries (SGXBs), if they contain a star luminosity class I-II. Another difference between BeXB and SGXBs is the accretion mode: the supergiant systems accreting from a radially outflowing stellar wind, and the BeXB binaries accreting from the circumstellar disc. For this reason, the supergiants are persistent sources of X-rays, while the BeX systems are transient and frequently much brighter (Bozzo et al. 2014).

1.3.1 Supergiant X-ray binaries (SGXBs)

Most of the so-called "classical" Supergiant X-ray binaries contains early-type supergiants as well as a neutron star (NS) accreting material from the strong radiative wind of its companion. These objects are persistent sources, with luminosities around $L_X \sim 10^{36}\ erg\ s^{-1}$,very variable on short timescales, but rather stable in the long run (Negueruela et al. 2006**)**. Orbital periods of these systems range from a few to tens of days (see, e.g., Chaty, 2013, for a recent review) while the spin periods are typically long, spanning from tens to several thousand seconds. A sub-class of SGXBs is the Supergiant Fast X-ray transients (SFXTs) (Ducci et al., 2014). SFXTs differ from SGXBs because they are only detected sporadically, during very brief outbursts.

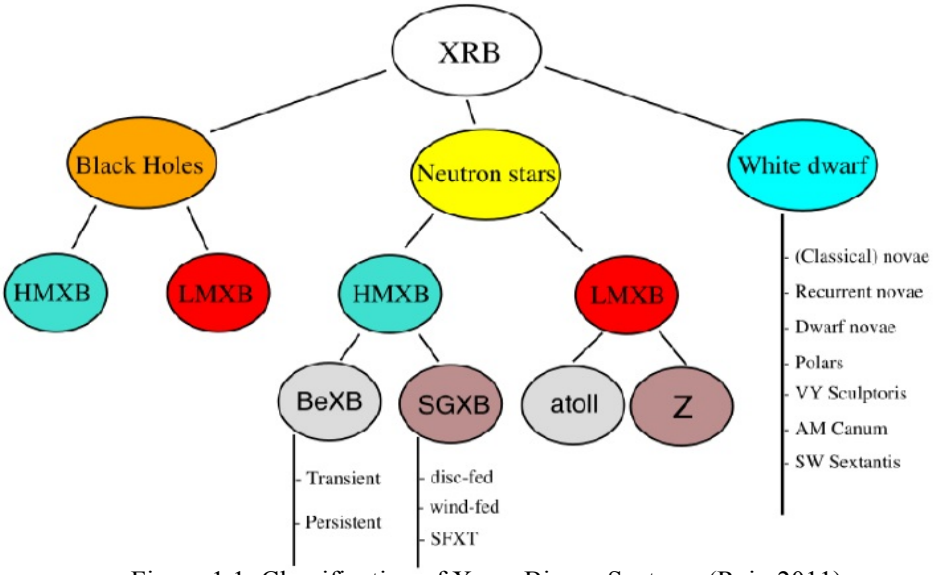

Figure 1.1: Classification of X-ray Binary Systems (Reig 2011)

1.3.2 Be/X-ray Binaries

These systems host a Be star in a relatively wide orbit (an orbital period of tens to hundreds of days) with a compact object, often a neutron star (Reig 2011) or less commonly a black hole (Munar-Adrover et al. 2014). A Be star is a non-supergiant fast-rotating B-type and luminosity class III-V stars. They show spectral lines in emission like those of hydrogen, He and Fe (see e.g Hanuschik 1996). Another observational signature of Be stars is the infrared (IR) excess from the circumstellar envelope. The origin of the IR is attributed to the electron-proton scattering in the circumstellar disc which produces free-free radiation from ionised gas (Woolf et al. 1970, Gehrz et al. 1974).

A very interesting study worth mentioning is Corbet´s diagram (1986). This diagram shows a strong correlation between the orbital and spin periods in BeXBs (see Fig. 1.2). Depending on their relation we can draw conclusions for the types of mass transfer. Specifically, we can see in figure 1.2 that the disc-fed SGXBs show an anticorrelation, as well as short orbital periods and short spin periods. The wind-fed SGXBs show no correlation or anticorrelation, as they have a flat distribution. As we see that the disc-fed SGXBs have also short orbital periods and short spin periods we can conclude that the Roche lobe overflow is the most likely mass transfer mechanism. The BeXBs show

a positive correlation between their orbital and spin periods. This correlation is understood in terms of equilibrium period. At this point and before we take further analysis to this manner of mass transfer we have to explain some terms.

Magnetospheric radius of a NS is the radius at which the magnetic stresses dominate the flow in the accretion disk.

Corotation radius called the radius at which material corotates with the NS at the Keplerian velocity.

Finally, **equilibrium period** is the period at which the magnetospheric radius and the corotation radius are equal and is given by

$$P_{eq} \propto B^{6/7} M_X^{-5/7} \dot{M}^{-3/7} \qquad (1.1)$$

where B, M_X and $\dot{M}$are the NS magnetic field strength, NS mass and the mass accretion rate, respectively; (Waters 1989)

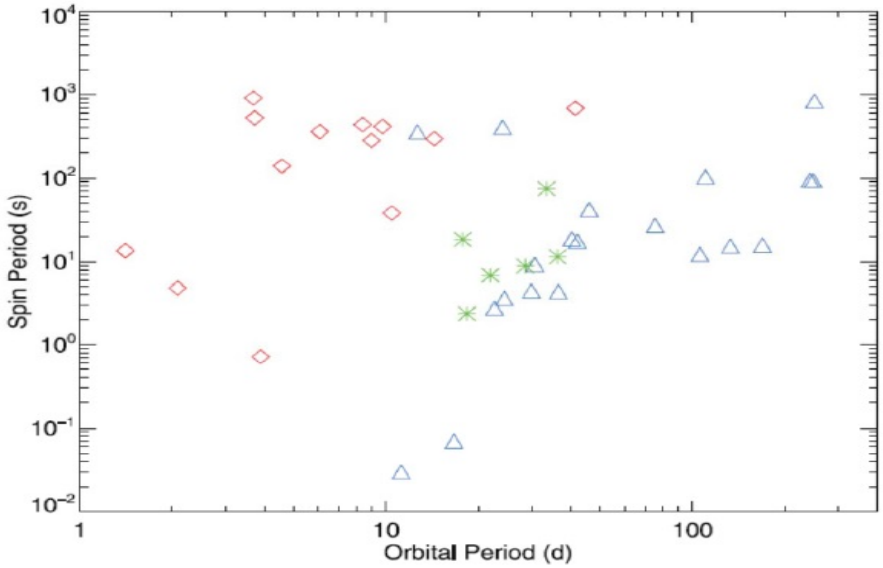

Figure 1.2: Corbet diagram for all the HMXBs that have known spin period excluding the PSR systems. The red diamonds represent the supergiant systems, the blue triangles are the Galactic Be/X-ray binaries and the green stars are the Small Magellanic Cloud Be/X-ray binaries (Townsend et al. 2011).

When the magnetospheric radius is smaller than the corotation radius, material accretes onto the NS, resulting in a decrease in the spin period (spin-up) since angular momentum is gain from the accreted material. Otherwise (in the case that the corotation radius is smaller than the magnetospheric radius), matter is spun away by the propeller mechanism resulting in an increase in the spin period (spin-down). The equilibrium period depends on the accretion rate because the accretion rate determines the size of

the magnetosphere. The higher the accretion rate, the smaller the magnetosphere. In turn, the accretion rate depends on the orbital separation of the two components of the binary system. The larger the orbital period the lower the amount of mass captured by the compact object.

1.3.2.1 Circumstellar Disk

Be stars are non-supergiant fast-rotating B-type stars characterized by Balmer emission (e.g. Ha) that originates in a circumstellar disk. The origin of their circumstellar disks is one of the longest-standing challenges in astronomy (Slettebak and Snow 1987; Smith, Henrichs, and Fabregat 1999; Porter and Rivinius 2003). Generally, disks displayed in astrophysical accretion systems, wherein they form as a means to provide outward viscous transport of the angular momentum of the infalling material (Shakura & Sunyaev 1973; Frank et al. 2002).

A phenomenological characteristic of Be stars is that they rotate rapidly. Specifically, the equatorial rotation velocity is close to the critical velocity (the velocity at which centrifugal forces balance Newtonian gravity at the equator) (Struve 1931). In a star rotating close to the critical velocity the effective equatorial gravity is reduced to the extent that weak processes such as gas pressure or non radial pulsations can easily eject matter into a Keplerian disc. The precise mechanism triggering this mass ejection remains elusive. The rotational velocity is usually estimated from the width of certain spectral lines. The problem is that if we take into account the gravitational darkening then for stars rotating above ~80% of critical speeds the relationship between the width of spectral lines and the rotational velocity is no longer valid. Actually, any increase in the rotational velocity is accompanied by almost no change in the line width (Collins & Truax 1995; Cohen et al. 2005).

1.3.2.2 Disk Loss Episodes

The disk in Be stars evolves (forms and dissipates) on time scales of years. The disk-loss episodes are a vey important event because they allow us to observe the underlying star wihout the contribution of the the disk emission. Because of the presence of the circumstellar envelope which surrounds the equator of the Be star, the determination of the spectral type and luminosity class in this case is not straightforward. The hydrogen free-bound and free-free processes in the circumstellar envelope cause the Be stars to appear redder than the non-emission B stars and distorts the photospheric spectrum. The only way to identify the real luminosity of the star is during of a disc loss episode by subtracting the luminosity taken from the star with the disk, we get the luminosity of the disk. The Hα line, during this episode, shows an absorption profile and at the time that the disk reappears the Hα line shows an emission profile (see Fig. 1.3).

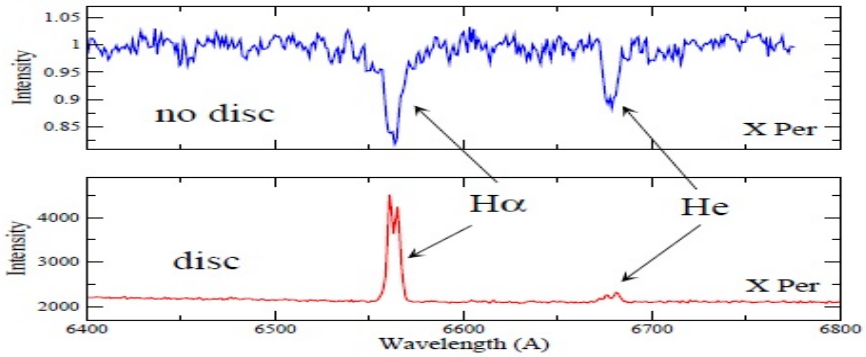

Figure 1.3: The H_α and H_e lines during absorption (blue diagram) and emission (red diagram) (Reig 2011)

1.3.2.3 X-ray variability of BeXBs

Because of the process of accretion, BeXBs are bright emitter of high-energy radiation. The material from the circumstellar disc is channeled by the magnetic field lines of the NS. Some of the material transported to the north magnetic pole and the other to the south magnetic pole. The material accelerated to high velocities because of the large gravitational well of the NS as a result of this a free-fall motion. When the material makes contact with the surface of the NS the kinetic energy is converted to thermal energy and is radiated away as X-rays.

BeXBs generally exhibit transient X-ray behavior, however persistent sources displaying weak X-ray emission have been reported (e.g. Reig & Roche 1999).

Persistent sources

According to Reig & Roche (1999) persistent sources has low X-ray luminosity and show flat light curves with sporadic and unpredicted increases in intensity. Their spin period is greater or equal than 200s and displays a weak iron line (sometimes this line does not even exist). A thermal excess of blackbody type, with high temperature (kT > 1 keV) and small emission area (R < 0.5 km), has recently been suggested as another common feature of this type of sources (La Palombara et al. 2009, and references therein).

Transient sources

In this type of source, we observe two manner of outburst activity (see Fig. 1.4):

1. Type I outbursts which concur during periastron passage. The luminosity can reach values up to $10^{37}\ ergs^{-1}$(Stella et all, 1986). Type I outbursts are generally separated by the orbital period of the NS and last for a relatively short duration (0.2-0.3 Porb, Reig 2007)

2. Type II outbursts which show no clear orbital modulation. In this type of outburst the luminosity can reach values close to the Eddington limit ($L_X \geq 10^{37} ergs^{-1}$) and have longer duration (last from weeks to months). The formation of an accretion disk may occur (Kriss et al. 1983; Motch et al 1991; Hayasaki & Ozakaki 2004; Wilson et al. 2008). The large and steady

spin-up rates seen during the giant outbursts support the formation of a transient accretion disk.

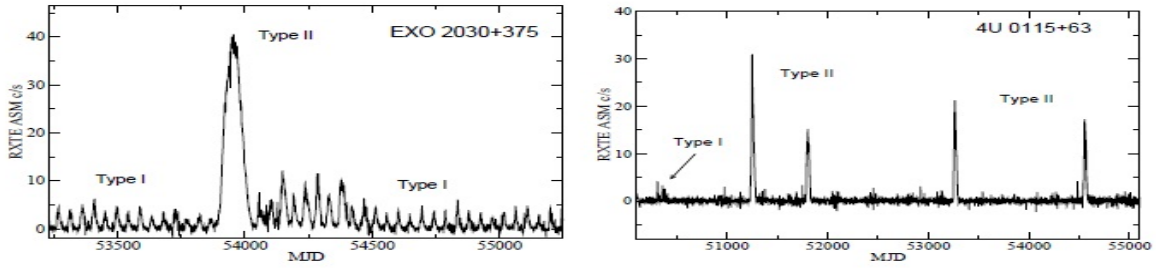

Figure 1.4: Typical light curves for Type I and Type II X-ray outbursts for two sources, EXO 2030+375 (left) and 4U 0115+63 (right). (Reig 2011)

1.4 Accretion

Accretion is a process that occurs when the objects of a binary star systems are close enough so the secondary star is tidally distorted and mass transfer is initiated. The extraction of gravitational potential energy from material which accretes on to a gravitating body is now known to be the source of power in several types of close binary systems and constitutes a powerful mechanism for producing high-energy radiation.

The gravitational potential energy released by the accretion of a mass m on to its surface is

$$\Delta E_{acc} = GMm/R_* \qquad (1.2)$$

According to this relation as much greater the ratio M/R_* is, the more effective the accretion as an energy release mechanism will be. For a fixed value of the compactness the luminosity of an accreting system depends on the rate $\dot{M}$at which matter is accreted. So we have the expression of accretion luminosity

$$L_{acc} = GM\dot{M}/\ R_* \quad (1.3)$$

We can re-write the 1.3 in terms of typical orders of magnitude: writing the accretion rate as

$$\dot{M} = 10^{16}\dot{M}_{16} g\ s^{-1} \quad \text{we have}$$

$$L_{acc} = 1.3\times10^{33}\dot{M}_{16}(M/M_\odot)(10^9 \text{ cm/ R}_*)\ erg\ s^{-1} \quad (1.4) \text{ for white dwarfs}$$

$$L_{acc} = 1.3\times10^{33}\dot{M}_{16}(M/M_\odot)(10 \text{ km/ R}_*)\ erg\ s^{-1} \quad (1.5) \text{ for neutron stars}$$

For a close binary systems involving these types of star $10^{16} g s^{-1}$ is a typical order of magnitude for accretion rates so we have $\dot{M}_{16} \sim 1$ and we expect for white dwarfs luminosity $10^{33}\ erg\ s^{-1}$and $10^{36}\ erg\ s^{-1}$for neutron stars.

1.4.1 Types of accretion

Binaries can transfer matter through three main ways. These are:

a) **Accretion via Roche lobe overflow**: In the course of its evolution, one of the two stars in a binary system may increase in radius, or the binary separation may shrink, to the point where the gravitational pull of the companion can gradually remove the outer layers of its envelope. This is called Roche lobe overflow.

b) **Stellar wind accretion:** Early-type stars are known to lose mass in the form of a stellar wind; some of this material will be gravitationally captured by the companion.

c) **Accretion from Be stars:** Accretion from the circumstellar envelope of a Be star.

1.4.1.1 Accretion via Roche lobe overflow

Edouard Roche was first studied the problem considering two auto-gravitating bodies orbiting around a common center of mass, which influence a gravitationally bound test mass. Around each star there are regions of space inside of which the gravitational force from star 1 is stronger than star 2 and reverse. These regions are called Roche lobes and are visible in the bottom part of the figure 1.5. The shape of each of the two Roche Lobes is like a teardrop, and they meet at the first Lagrangian point L1 in which the gravitational force from both stars is exactly equal and the matter can go from being bound to one star to the other**.** This accreting matter has a high angular momentum which must be conserved so it can not be directly captured by that star but it will rotate around it forming an accretion disk.

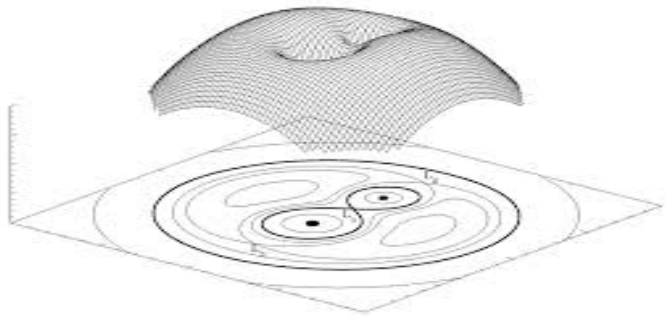

Figure 1.5: A three-dimensional representation of the Roche potential in a binary star. At the Lagrangian points L1, L2 and L3 forces cancel out .- http://hemel.waarnemen.com/Informatie/Sterren/hoofdstuk6.html\#mtr.

1.4.1.2 Stellar wind accretion

Early-type stars (O or B) are known to lose mass in the form of a stellar wind which can be accumulated by the second star as it moves on its orbit through this wind (see Kudritzki & Puls 2000, for a review). Material is accelerated outwards from the stellar atmosphere to a final velocity u_∞ according to a law that may be approximated as

$$u_w(r) = u_\infty \left(1 - \frac{R_*}{r}\right)^\beta \quad \text{(I. Negueruela, 2009).}$$

Where R_* is the radius of the donor star and β is a factor lying in the interval ~ 0.8 − 1.2. Since under these conditions the wind is highly supersonic and its speed is much higher than the orbital velocity of the neutron star we can approximate to the accretion process using the Bondi-Hoyle-Lyttleton formulation (more information about Bondi-Hoyle-Lyttleton formulation in the review by Edgar (2004)). According to this formulation the maximum distance at which gravitational potential of a neutron star which is dipped in a fast wind well can deflect the stellar wind and focus the outflowing material towards the neutron star is call accretion radius and and is given by

$$r_{acc} \sim \frac{2GM_x}{u_{rel}^2}$$

where u_{rel}^2 is the relative velocity of the accreting mass and is $u_{rel}^2 \approx u_w^2 + u_{orb}^2$ and r_{acc}~$10^8\, m$. Accretion rate is given by

$$\dot{M} = 4\pi (GM_X)^2 \frac{u_w(r)\rho(r)}{u_{rel}^2}$$

where ρ(r) is the wind density.

Finally, the X-ray luminosity is given by

$$L_X \sim \dot{M} \sim \frac{u_w(r)\rho(r)}{u_{rel}^4} \quad (1.6)$$

from which we see that the X-ray luminosity is constant only in a circular orbit and changes in an eccentric orbit.

1.4.1.3 Accretion from Be stars

When the B-star goes through a B-emission phase and ejects matter from its equator, part of this is captured at a distance r_{acc} by the NS. This accretion mechanism is more efficient when the system eccentricity is low as the NS passes closer to the Be star and in a denser region around it. The accretion mechanism is about the same as the case of stellar wind accretion and the same description can be assumed to work as a first approximation. The main difference is that the material captured from a circumstellar disk has a lower velocity and higher density than that from a stellar wind, which results in higher X-ray luminosity.

1.5 Spectral states in Be/X-ray pulsars

Reig and Nespoli (2013) studied all BeXBs (except 4U 1901+03 BeXB) that went into outburst during the life time of the RXTE mission. They searched for correlations of the color, spectral and timing parameters as a function of X-ray flux and between various spectral parameters. More specifically these parameters are the soft (SC) and hard (HC) colors, the photon index (Γ), the cutoff energy (E_{cut}), the energy (E_{Fe}) and intensity (I_{Fe}) of the iron line.

Some of the result from this study which are relevant to the present work are the following:

- The photon index anticorrelates with X-ray flux in the HB and correlates with it in the DB.

- The cutoff energy shows the same behavior as the photon index; it increases as the flux decreases in the HB and increases as the flux increases in the DB. Therefore, there is a positive correlation between the photon index and the high-energy cutoff.

- The fluorescent iron Kα line is created by reflection of hard X-rays from the nH absorption. As the ionization stage increases so does the energy of the line. Because of the energy separation is so small can be thought as part of the 6.4 keV blend (Ebisawa et al. 1996; Liedahl 2005).

The study of Reig and Nespoli (2013) showed also the existence of two spectral branches in accreting X-ray pulsars: *horizontal branch (HB)*, a low-intensity and highly variable state and *diagonal branch (DB),* a high-intensity state. These two branches are clearly identified in the hardness-intensity diagram (a plot of 2-30 kev band count rate as a function of hardness which is defined by the ratio of the fluxes in the 7-10 kev/ 4-7 kev energy bands (see Fig 1.6)). The HB correspond to a low-intensity state (at the beginning or end of an outburst), while the DB corresponds to a high-intensity state. When the X-ray luminosity goes above a critical limit, the source makes a sudden turn in the HID and undegoes a transition from the HB to the DB. If a source displays only the HB, then the peak of the outburst corresponds to the hardest spectrum. Reig and Nespoli (2013) proposed that the two branches correspond to the two different accretion modes (see below) and which are depending on whether the luminosity of the source is above or below a critical value. Specifically, when a source displays the HB branch ***(SUB-CRITICAL)*** then the deceleration of the flow to rest at the stellar surface is accomplished via Coulomb interactions. On the other hand, when a source displays the DB branch ***(SUPERCRITICAL)*** then the deceleration occurs via by the pressure of the radiation field. The value of the critical luminosity depends the pulsar magnetic field as a result the luminosity at which the transition takes place varies across different sources. For typical values of the magnetic field in Be/X-ray pulsars, the critical luminosity is expected to be of the order of a few times $10^{37}\ erg\ s^{-1}$.

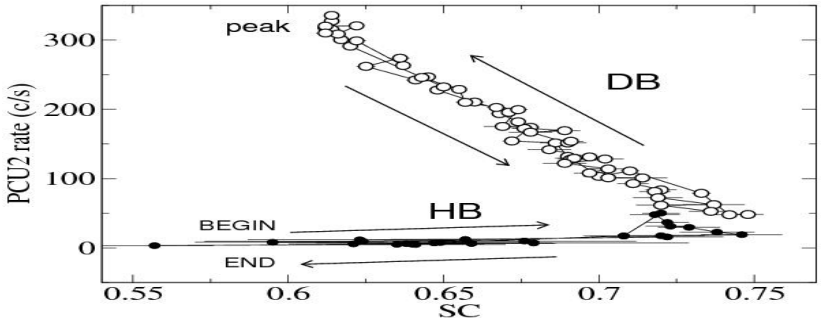

Figure 1.6: Hardness-intensity diagrams. (Reig 2013)

1.6 The accretion column

The accretion disc formed in the neutron star by the infalling flow of matter spiraling around it until the pressure of the star's dipole magnetic field becomes comparable to the ram pressure of the matter in the disk. This happens at the Alfven radius where the accreted matter is funneled along the magnetic field lines and moves down to the magnetic poles in a symmetric column. The observed X-ray emission is a result of the conversion gravitational potential energy into kinetic energy and then into radiation via electron scattering. After the matter is captured by the magnetic field of neutron star there are two ways to rest at the neutron star surface:

a) Matter can be dominated by radiation pressure.

b) Coulomb interactions (Basko & Sunyaev 1976)

There is a critical luminosity L_{crit} that determines the manner in which the matter settles on the neutron star surface. If the luminosity of a source is greater than the critical luminosity ($L_X > L_{crit}$) the source is supercritical and the deceleration of the flow to rest at the stellar surface is accomplished by the pressure of the radiation field. On the other hand, if the luminosity of a source is less than the critical luminosity ($L_X < L_{crit}$) the source is subcritical and the deceleration occurs via Coulomb interactions (see Fig. 1.7).

According to Becker et al. (2012) these two different regimes can explain the bimodal behavior of the variability of the cyclotron energy with luminosity; The data from both long-term and short-term (pulse-to- pulse) observations shows that in the supercritical sources the centroid energy of the cyclotron resonant scattering feature (see 1.7) is negatively correlated with luminosity while in the subcritical sources the opposite behavior is observed. The critical luminosity can be estimated as (Becker et al. 2012)

$$L_{crit} \approx 1.28 \times 10^{37} (E_{cyc}/10kev)^{16/15} \, erg \, s^{-1} \quad (1.7)$$

1.6.1 Supercritical sources

In the supercritical sources the pressure of the radiation field is big enough to decelerate the infalling gas to rest at the stellar surface. This procedure begins when the freely-falling material encounters a radiation-dominated shock at a certain altitude. Below the shock, the photons are trapped by advection, although they eventually manage to escape by diffusing through the walls of the column forming a "fan beam". So the observed radiation escape from a lower altitude than shock altitude.

1.6.2 Subcritical sources

In the subcritical source, the matter passes through a radiation-dominated shock, begins to decelerate but the pressure of the radiation is insufficient to bring the matter to rest at the stellar surface (Basko & Sunyaev 1976). In this case the final deceleration occurs via Coulomb interactions close to the base of the accretion column (Burnard et al. 1991) and the emission escapes from the top of the column, forming a "pencil beam".

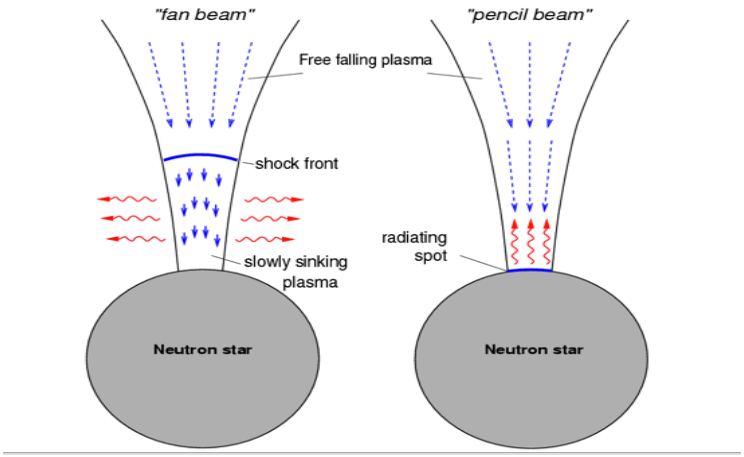

Figure 1.7: Left: *fan beam*. Right: *pencil beam* (Kretcshmar 1996)

1.7 Cyclotron resonant scattering features

In the X-ray spectra of many XRB Cyclotron resonant scattering features (CRSF) have been observed in the form of absorption line. This features are caused by scattering of X-ray photons from electrons in the accreting plasma channeled by the NS magnetic field. The strength of the magnetic field can be estimated from the energy of cyclotron resonant scattering features (CRSF) through the relation

$$Ecyc = 11.6 \frac{B}{10^{12} G} (1+z)^{-1} keV \quad (1.8)$$

where B is the magnetic field and z is the gravitational redshift.

As mentioned above, in the supercritical sources the centroid energy of the CRSF is negatively correlated with luminosity while in the subcritical sources the opposite behavior is observed (Becker et al 2013).

1.8 4U 1901+03

4U 1901+03, the source, which is the subject of this thesis, was discovered by Uhuru and Vela 5B (Forman et al. 1976; Priedhorsky & Terrell 1984) when it went into outburst in 1970–1. In 2003 February a new outburst of 4U 1901+03 was detected by the All-Sky Monitor (ASM) aboard RXTE (Galloway et al. 2003b). The source was also detected with the IBIS and JEM-X hard X-ray instruments aboard INTEGRAL

between 2003 March 10 and April 13 2003 (Molkov et al. 2003). During the second giant outburst, the X-ray flux of the source reached a value of $F \sim 8 \times 10^{-9} ergs\, cm^{-2} s^{-1}$. X-ray flares with a duration of 100–300s had been observed during the peak of this outburst. Near the end of the outburst, a QPO at ν=0.135 Hz was detected (James et al., 2010). The orbital period and eccentricity of the system are measured as 22.58 d and 0.035, respectively. The period of X-ray pulsation is about 2.73 s (Galloway et al. 2005). With the observation of RXTE Proportional Counter Array (PCA), Galloway et al. (2003a) obtained coordinates of R.A.= $19^h03^m37^s$, Dec=$+3^0 11' 31''$. No optical or IR counterpart has been found for this source so far (Galloway et al. 2005). Galloway et al. (2005), based on the RXTE observations, studied the orbital parameters, the pulse profiles from several observations during the 2003 giant outburst. Chen et al. (2008) found that the pulse profile is correlated with both, the X-ray luminosity and photon energy. Finally, Lei et al. (2009) present for the first time phase-resolved spectra of 4U 1901+03 using all available RXTE data taken during the 2003 giant outburst. They found that the iron line at 6.4 kev, caused by the illumination of neutral or partially ionized material in the surroundings of the X-ray source did not vary with pulse phase, which indicates that the iron emission comes from a region in the accretion disk rather than the surface of the neutron star.

Aim for this project

In this project we present a detailed X-ray and optical study of the 4U 1901+03. The aim of the project is to investigate the accretion regime that the source went through the 2003 outburst and study the existence of spectral states in the framework of Reig and Nespoli (2013). We have performed the most detailed X-ray spectral analysis of the evolution of the spectral parameters with time and flux carried out so far. Particular attention was given to the so-called "10-keV feature", a deficit of photons around 10 keV that has been detected in a number of X-ray pulsars. In this work, we discuss whether this feature can be attributed to a cyclotron line. Finally, we attempted to identify the optical counterpart to 4U 1901+03 through the analysis of optical and IR photometry.

Chapter 2

Observations and Data analysis

2.1 Observations

2.1.1 X-ray observations

The data that we used for the X-ray spectral analysis were obtained with the instruments on board the Rossi X-ray Timing Explorer (RXTE) satellite from February 10 to July 16 2003.

RXTE (see Fig. 2.1) observes the sky in a broad energy band of 2–200keV (Bradt et al. 1993). RXTE is used for the observation of X-ray sources in a wide energy range with a time resolution of microseconds. The spacecraft carried two pointed instruments, the Proportional Counter Array (PCA) to cover the lower part of the energy range and the High Energy X-ray Timing Experiment (HEXTE) to cover the upper energy range.

The PCA instrument consists of five Proportional Counter Units (PCU) giving a total collecting area of 6500 cm^2 and covers an energy range of 2-60 keV. The 5 Proportional Counter Units (PCUs) are filled with xenon gas and have an anticoincidence system and a propane top layer to reduce the background. It provides an energy resolution of 18% at 6 keV (Jahoda et al. 1996).

The High Energy X-ray Timing Experiment (HEXTE) consists of 2 clusters of 4 NaI/CsI scintillation counters that together have a total effective area of 1600 cm^2 and covers an energy range of 15–250 keV band with a nominal energy resolution of 15% at 60 keV (Rothschild et al. 1998). The extent of the collecting area is about 2 × 800 cm^2.

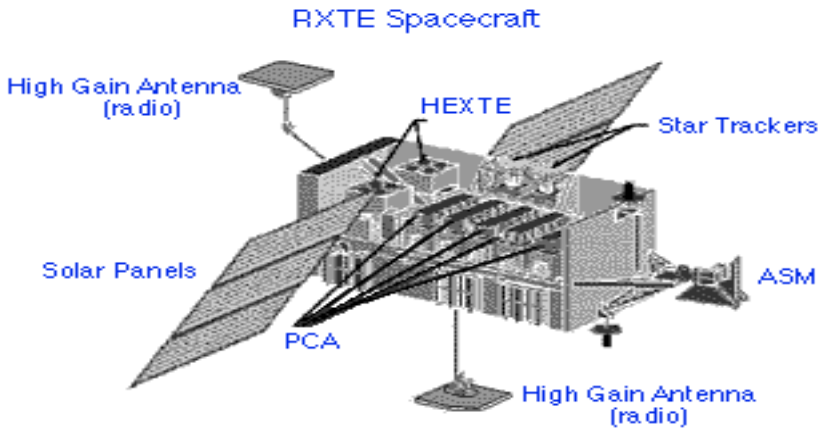

Figure 2.1: RXTE satellite.-http://heasarc.nasa.gov/docs/xte/learning_center/what_is_RXTE.html

2.1.2 Optical observations

The optical observations were made from the Skinakas Observatory on 22 July 2015, located in the island of Crete (Greece). The 1.3m telescope is the principal observing facility of Skinakas Observatory (see Fig. 2.2). It is a modified Ritchey-Chretien telescope that has a hyperbolic primary and a hyperbolic secondary mirror, so it can provide a large field of view with high image quality. Also there is an auto guider with off axis guiding system. Some technical details of the telescope are cited below:

• Aperture of main mirror: 129cm

• Aperture of secondary mirror: 45cm

• Central hole of main mirror: 35cm

• Distance main to secondary: 245.34cm

• Focal length: 985.7cm

• F-ratio: 7.64

Figure 2.2: Skinakas 1.3m telescope

The CCD (Charge Couple Device) that was used for the photometry is the ANDOR DZ436. Some of the characteristics of the camera are listed below:

- Active pixels: 2048 x 2048
- Pixel size (WxH; μm):13.5x13.5
- Cooling down to -75^{o}C.

- FOV 9.5Arcmin square

We used the Johnson-Cousins B, V, R, and a narrow Ha filter (see table 2.1).

Standard Johnson-Cousins filters						
Type	Central Wavelength (Å)	FWHM (Å)	Peak Transmission (%)	Diameter (mm)	Thickness (mm)	Manufacturer
U	3640	320	63	75.9		Custom Scientific
B	4350	980	72	75.9	8.9	Custom Scientific
V	5380	980	88	75.9	8.9	Custom Scientific
R	6300	1180	82	76.0	9.1	Custom Scientific
I	8940	3370	96	75.9	8.9	Custom Scientific

Table 2.1: Johnson-Cousins filter (http://skinakas.physics.uoc.gr/en/index.html)

2.2 Data analysis

2.2.1. Spectral analysis

We used the data of Standard-2 mode of PCA and *Standard (archive)* mode of the HEXTE to perform the spectra analysis and extract the total lightcurve. A systematic error of 0.6% was added to the spectra to account for the calibration uncertainties. For each observation, we fitted the two spectra simultaneously covering an overall 2–100 keV energy range with a multi-component model.

For the spectral fitting we used the XSPEC 12.5 version. The spectrometer obtains the observed spectrum which is related to the actual spectrum of the source (f(E)) by:

$$C(I)= \int_0^\infty f(E)R(I,E)dE$$

where C is the photon counts within specific instrument channels, (I) , and R(I,E) is the instrumental response. The XSPEC included model spectrum, f(E), described in terms of a few parameters that the program adjusts in order to find the best-fit model for the observed spectrum. For each f(E), a predicted count spectrum (C_p(I)) is calculated and compared to the observed data (C(I)). Then the model parameters are varied to find the parameter values that give the best-fit statistics or the "best-fit model", which is defined by the minimum x^2 defined as follows:

$$x^2=\sum \left(C(I) - C_p(I)\right)^2 /(\sigma(I))^2$$

where σ(I) is the error for channel I and is usually estimated by $\sqrt{C(I)}$. How good the fit is, depends on the number of degrees of freedom ν, which is defined as the number

of channels minus the number of independent model parameters. As a general rule, the fit is good when the x^2/ν is approximately equal to one and the parameters values are physical.

Table 2.2 gives the photon distribution for the different models. To fit the spectral continuum, we used a model composed by a combination of the following components:

- Photoelectric absorption (Balucinska-Church & McCammon 1992). The photoelectric absorption in Xspec defined as PHABS. The parameter of this component is the hydrogen column density, n_H. The value of n_H cannot be precisely constrained because of the low effective area PCA below 3 keV (Ya-Juan Lei et al. 2009).

- A power law with high-energy exponential cutoff (CUTOFFPL) to describe the spectral continuum of the source. The spectral parameters of this component are the photon index (i.e. exponent of the power law, Γ), the cutoff energy, E_{cut}, which describes the roll over that is observed at high energies, and the normalization K.

- A gaussian component (GAUSS) centered at 6-7 keV because of fluorescent Fe line emission. The parameters of this component are the line's central energy, E_l, width, σ, and the normalization K´ which corresponds to the intensity I_{Fe}.

- An absorption gaussian component which fits the spectrum in the range 8-12 keV and whose origin is unclear. This feature is defined as GABS and the parameters of this component are the E_0 which describes the central energy of the absorption line in kev E_0, the σ_0 width of the absorption line in kev and the S which is the line depth. This component will be referred to as the "10-keV feature".

The results of the fits can be found in the Appendix.

PHABS	$M(E)= \exp[n_H \sigma(E)]$
CUTOFFPL	$A(E)=KE^{-\Gamma}\exp\left[\frac{-E}{E_{cut}}\right]$
GABS	$M(E) = exp\left[-\left[\frac{S}{\sqrt{2\pi}\sigma_0}\right] exp\left[-0.5\left[\frac{(E-E_0)}{\sigma_0}\right]^2\right]\right.$
GAUSS	$A(E)=K'\frac{1}{\sigma\sqrt{2\pi}} exp\left[\frac{-(E-E_l)^2}{2\sigma^2}\right]$

n_H: equivalent hydrogen column (in units of 10^{22} atoms cm^{-2}).
K,K´: normalization in photons ke V^{-1} cm^{-2} s^{-1} at 1 kev. K´ is the intensity of the iron line (I_{Fe}).
Γ: power-law photon index.
E_{cut}: cut-off energy in keV.
S: line depth.
σ_0: width of the absorption line in keV.
E_0: central energy of the absorption line in keV.

E_l: iron line energy in keV.
σ: iron line width in keV.

Table 2.2: The spectra were fitted with a function of the above components.

2.2.2 Lightcurves and Hardness-intensity diagrams

The lightcurves and hardness intensity plots were created using a package of the HEASOFT-6.16 named XRONOS. More specifically the task named **lcurve** was used. Table 2.3 shows the observation date, the observation ID, the exposure time, the hardness ratio (HR) which is the ratio of the fluxes in the 7-10 kev/ 4-7 keV energy bands. We use HR to make the HID, a plot of 2-30 keV band count rate as a function of hardness, one point per RXTE observation.

Date (d-m-y)	JD	OBSID	Exposure time (s)	HR (7-10kev/4-7kev)	Flux at 2-100 kev (erg $cm^{-2}s^{-1}$)
10/2/03	52680.3367	70096-01-01-00	1712	6.33E-01	7.0537E-9
10/2/03	52680.4044	70096-01-01-01	1536	6.32E-01	6.90E-09
12/2/03	52682.5116	70096-01-01-02	1408	6.39E-01	7.58E-09
13/2/03	52682.9503	70096-01-01-03	5184	6.48E-01	7.67E-09
14/2/03	52684.7277	70096-01-03-00	13072	6.52E-01	8.32E-09
15/2/03	52685.5164	70096-01-03-01G	10352	6.52E-01	8.45E-09
17/2/03	52687.0344	70068-22-01-01	8384	6.53E-01	8.32E-09
17/2/03	52687.2392	70096-01-03-02	1776	6.50E-01	8.59E-09
17/2/03	52687.444	70068-22-01-02	11200	6.52E-01	8.66E-09
18/2/03	52688.4227	70096-01-03-03	1984	6.51E-01	8.74E-09
18/2/03	52688.5709	70068-22-01-03G	7232	6.51E-01	8.60E-09
19/2/03	52689.5462	70096-01-03-04	1936	6.49E-01	8.64E-09
19/2/03	52689.6888	70096-01-03-05	992	6.46E-01	8.60E-09
20/2/03	52689.8746	70068-22-01-04	10432	6.50E-01	8.35E-09
21/2/03	52691.0094	70096-01-04-00	3984	6.50E-01	7.91E-09
22/2/03	52692.0336	70096-01-04-01	3216	6.56E-01	8.47E-09
23/2/03	52693.7486	70096-01-04-02	2240	6.44E-01	8.52E-09
25/2/03	52694.9929	70096-01-04-03	3376	6.42E-01	8.04E-09
26/2/03	52696.3144	70096-01-04-04	2784	6.41E-01	8.42E-09
3/3/03	52701.0722	70096-01-05-00	1152	6.37E-01	7.59E-09
9/3/03	52707.9748	70096-01-06-00	1472	6.27E-01	7.62E-09
13/3/03	52711.1327	70096-01-06-01	1488	6.20E-01	7.59E-09
15/3/03	52713.8099	70096-01-07-00	3840	6.12E-01	7.01E-09

19/3/03	52717.0994	70096-01-07-01	3280	6.15E-01	7.05E-09
23/3/03	52721.0596	70096-01-08-00	1936	6.10E-01	7.00E-09
27/3/03	52725.4179	70096-01-08-01	928	6.17E-01	6.71E-09
30/3/03	52728.8761	70096-01-09-00	3392	6.10E-01	6.64E-09
2/4/03	52731.9762	70096-01-09-01	2480	6.09E-01	6.23E-09
4/4/03	52733.9481	70096-01-10-00	2752	6.06E-01	6.23E-09
8/4/03	52737.8907	70096-01-10-01	1232	6.01E-01	6.28E-09
11/4/03	52740.8481	70096-01-11-00	3296	6.11E-01	6.02E-09
14/4/03	52743.8736	70096-01-11-01	3360	6.04E-01	5.64E-09
18/4/03	52747.1001	70096-01-12-00	2912	6.05E-01	5.95E-09
22/4/03	52750.9766	70096-01-12-01	3408	6.06E-01	5.62E-09
25/4/03	52754.6625	70096-01-13-00	2496	6.06E-01	5.15E-09
30/4/03	52759.0659	70096-01-13-01	1568	6.03E-01	4.88E-09
30/4/03	52759.1611	70096-01-13-02	720	6.02E-01	4.78E-09
3/5/03	52762.9462	70096-01-14-00	3232	6.04E-01	4.64E-09
6/5/03	52765.9059	70096-01-14-01	3408	5.99E-01	4.27E-09
13/5/03	52772.8777	70096-01-15-01	2704	5.99E-01	3.84E-09
17/5/03	52776.8312	70096-01-16-00	2704	5.98E-01	3.64E-09
21/5/03	52780.5055	70096-01-16-01	3424	5.94E-01	3.32E-09
25/5/03	52784.3201	70096-01-17-00	3216	5.86E-01	3.02E-09
29/5/03	52788.6172	70096-01-17-01	1392	5.75E-01	2.52E-09
1/6/03	52791.4216	70096-01-18-00	1680	5.74E-01	2.47E-09
1/6/03	52791.7077	70096-01-18-02	1248	5.72E-01	2.38E-09
4/6/03	52794.1131	70096-01-18-01	3072	5.72E-01	2.32E-09
6/6/03	52796.8177	70096-01-19-00	3040	5.76E-01	2.07E-09
10/6/03	52800.7601	70096-01-19-01	2320	5.69E-01	2.00E-09
14/6/03	52804.4496	70096-01-20-00	1536	5.78E-01	1.73E-09
18/6/03	52808.5179	70096-01-20-01	2752	5.63E-01	1.41E-09
21/6/03	52811.5429	70096-01-21-00	2880	5.77E-01	1.20E-09
25/6/03	52815.6396	70096-01-21-01	1568	5.75E-01	1.07E-09
28/6/03	52818.4459	70096-01-22-00	2448	5.92E-01	9.22E-10
2/7/03	52822.3248	70096-01-22-01	1824	6.22E-01	6.61E-10
5/7/03	52825.7568	70096-01-23-00	2352	6.41E-01	3.00E-10
8/7/03	52828.0722	70096-01-23-02	992	6.11E-01	2.15E-10
9/7/03	52829.9051	70096-01-23-01	1776	6.36E-01	1.13E-10
12/7/03	52832.1486	70096-01-24-00	944	4.81E-01	1.12E-11
13/7/03	52833.1994	70096-01-24-02	1200	4.72E-01	3.29E-11
14/7/03	52834.1836	70096-01-24-01	1360	4.69E-01	2.67E-11
15/7/03	52835.6336	70096-01-24-03	352	4.37E-01	2.73E-11

Table 2.3: RXTE observations

2.2.3 Photometry

The aim of these observations was the searching of the optical counterpart to 4U 1901+03 source. We used two methods for this searching:

1) Optical photometry. The first method that we used is described in the study of Reig et al. (2005). According to this study, we can identify the optical counterpart of a BeXB from the color-color diagram (the red color ($R - H\alpha$) as a function of the blue color ($B - V$)) and more specifically to look for the presence of Hα in emission in the uncertainty region provided by the X-ray observations (as an example see Fig. 2.3). The size of the X-ray error radius of the source reported in this work was ~1′. The fields around the best-fit X-ray position were observed through the *B*, *V*, R filters and a narrow filter centred at 6563 Å (Hα filter). Because we are looking for early-type stars (low $B-V$ colours) with moderately and or large Hα excess (that means larger $R - H\alpha$ colours) we expect that stars occupy the upper left parts of the diagram. Reduction of the data was carried out using the IRAF tools for aperture photometry. Before extracting the instrumental magnitudes, the images have to be corrected for BIAS and FLAT-FIELD. The first step is to subtract the BIAS level from the raw images. BIAS frames are images of zero second exposure time obtained with the telescope's shutter closed. In that way, the noise due to the camera electronics can be removed. Then, the raw images were FLAT field corrected. This process is used to correct for the different spectral response of the pixels.

   Stars were detected using the DAOFIND task which automatically find stars using an algorithm. Table 2.4 shows some of the parameters we used for this procedure.

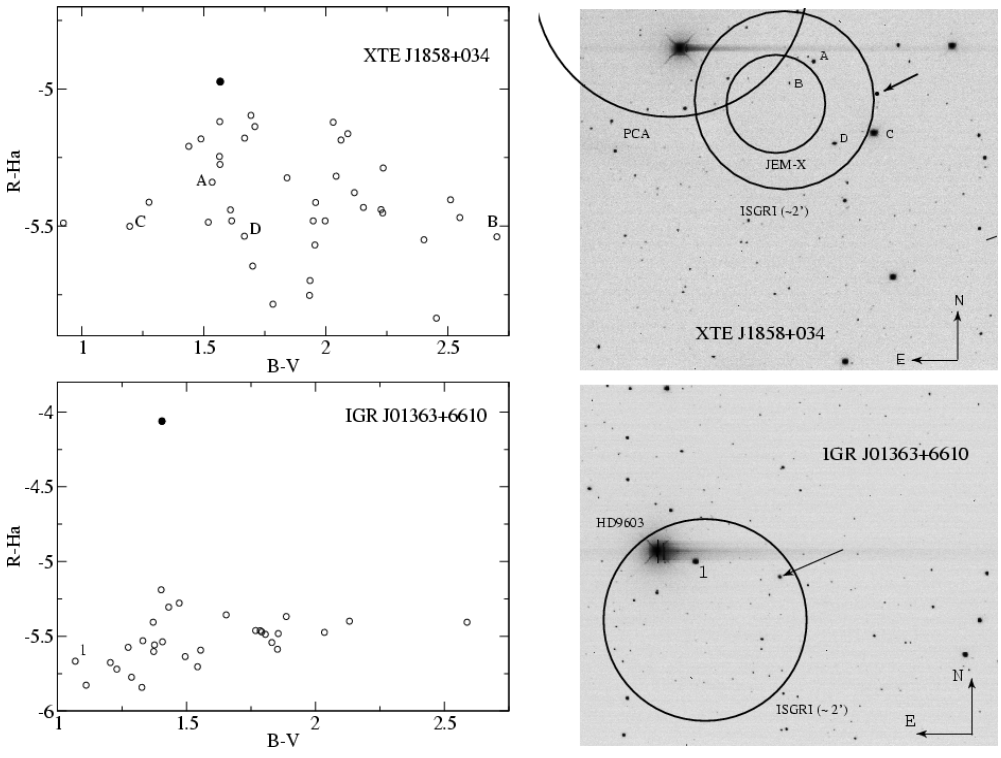

Figure 2.3: Color-color diagrams and V-band images of the field around XTE J1858+034 (top) and IGR J01363+6610 (bottom). For XTE J1858+034, the 2.5′ PCA RXTE ,2′ ISGRI INTEGRAL and 1′ JEM-X INTEGRAL radius error circles are shown. For IGR J01363+6610, the 2′ ISGRI INTEGRAL error circle is shown. The proposed optical counterparts are marked with a filled circle on the diagrams and with an arrow on the images (Reig 2005).

Full Width Half Max (FWHM)	4 pixels
Threshold	10 counts
Standard deviation of background in counts	15 counts
Inner radius of sky annulus in scale units	19 pixels
Width of the sky annulus in scale units	5 pixels
Aperture radii in scale units	15 pixels
Centering box width in scale units	8 pixels
Minimum good data value	10
Maximum good data value	55000
Itime (exposure time)	1200s for B filter 900s for V filter 600s for R filter 1500s for Ha filter

Table 2.4: Apphot parameters

1) Infrared photometry (Negueruela & Schurch 2007) . This method is similar to the previous one with the difference being that we use datasets at other wavelengths. Specifically, we use 2MASS photometric data to search for objects within the X-ray error circle. 2MASS (Two Micron All Sky Survey Extended Catalog) was a grounded-based survey between 1997-2001 (Skrutskie et al. 2006), covering the 99.998% of the celestial sphere and precise photometry over the entire sky in the near infrared J (1.25μm), H (1.65μm) and

K_S (2.16 μm) bandpasses (Bilicki et al 2013). 2MASS used two 1.3-m telescopes, one at Mt. Hopkins, AZ, and one at CTIO, Chile. Because of the assumption of a standard reddening law, which is much more likely to hold in the infrared than in the UV/optical region (e.g., Indebetouw et al. 2005), Negueruela & Schurch (2007) defined the reddening-free quantity

$$Q=(J-H)-1.70(H-K_S)$$

and created Q/K_S diagrams to separate early type from late type stars. For stars K> 12 the photometry is not reliable due to the accuracy of the observations. Thus the early B stars in the K-Q diagram is defined by $K_s<12$ and $Q<0$ (see as an example Fig. 2.4).

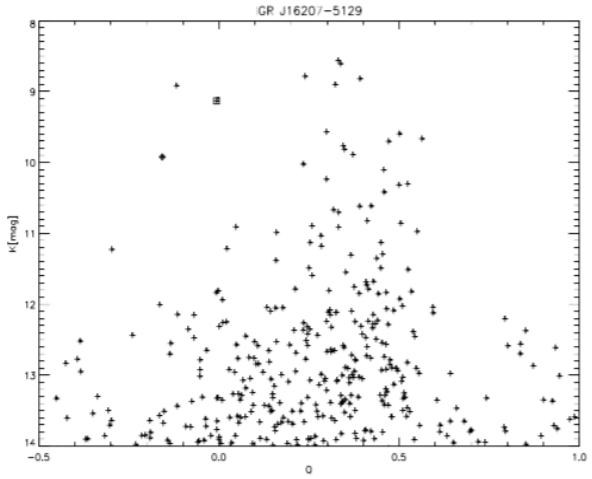

Figure 2.4: A plot of IR *Q* values against K_S magnitude for 2MASS stars within 3′ of the position for IGR J16207−5129. Candidate early-type stars stand out on the top left corner (Negueruela & Schurch 2007).

Chapter 3

Results

In this Chapter we present the results of our X-ray and optical analysis of the accreting X-ray pulsar 4U 1901+03. The key questions we wish to investigate are whether 4U 1901+03 display X-ray states and how the spectral parameters evolve during the X-ray outbursts. With respect to the optical analysis, we try to identify the optical counterpart, which remains undetected in the optical band.

3.1 X-ray states

The light curve of 4U 1901+03 covering 150 days is presented in the figure 3.1. The outburst started around JD 52680 and reached a maximum count rate of 608 counts s^{-1} for one PCU at JD 52694 then it declined linearly reaching a count rate of about 2 counts s^{-1} for one PCU at JD 52834. The decay is fairly linear, which is somehow unusual for a BeXB. Figure 3.2 shows a linear fit to the decay using the Method of Least Squares. We found that the decay rate is -4.37 $\frac{c/s}{day}$.

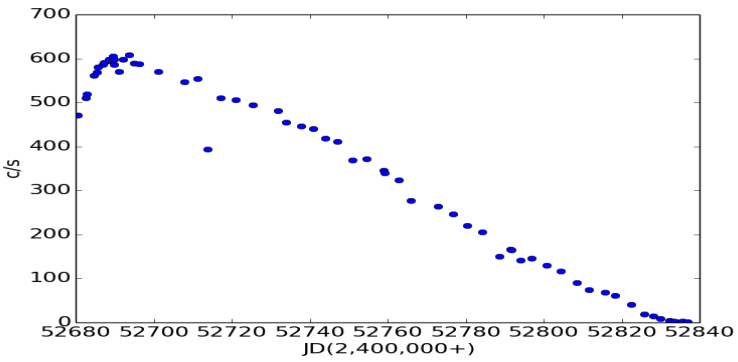

Figure 3.1: The light curve of 4U 1901+03

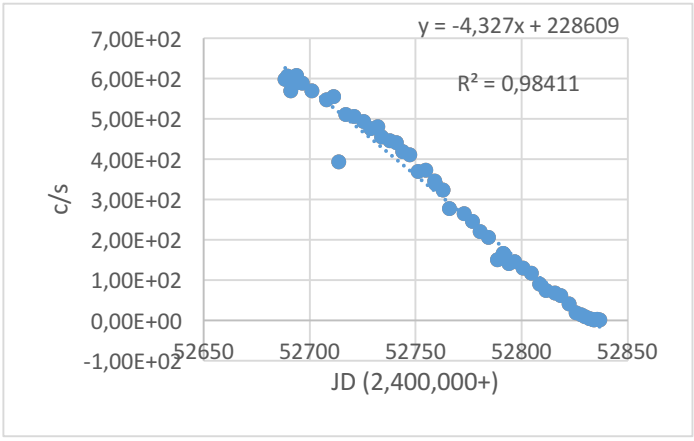

Figure 3.2: The linear fit to the decay of the outburst using the Method of Least Squares .

Figure 3.3 shows the Hardness-Intensity Diagrams of the 4U1901+03 which is a plot of 2-30 keV band count rate as a function of hardness which is defined by the ratio of the fluxes in the 7-10 keV/ 4-7 keV (HR). When the outburst begins, the system moves rightward on the HID and the hardness increases. After the peak luminosity is reached, the hardness starts decreases as the system moves leftward on the HID. When the flux gets to $\sim 1.5\times10^{-9} ergs^{-1}$ the source makes a sudden turn in the HID and the hardness starts to increases again. Finally, we see a last turn when the flux gets to $\sim 3.0\times10^{-10} ergs^{-1}$ where the hardness starts decreases for a last time.

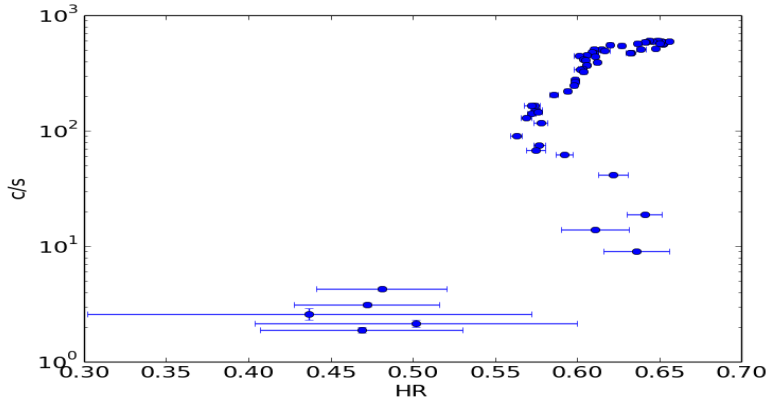

Figure 3.3: Hardness-Intensity Diagrams of the 4U1901 +03

3.2 Evolution of the spectral parameters.

The energy spectra of 4U1901+03 were fitted with the models of XSPEC discussed in Chapter 2. Figure 3.4 shows two spectra of the source for two flux levels while in figure 3.5 we fit the spectral continuum of the source without using the absorption gaussian component. According to this diagram the absorption gaussian component is necessary for the fitting.

The diagrams of the different spectral parameters as a function of the X-ray flux at 2-100 keV are presented bellow. The diagram of the equivalent hydrogen column n_H (PHABS model) over X-ray flux is shown in figure 3.6. In figure 3.7 we see the diagrams of the parameters of the CUTOFFPL model which are cutoffpl photon index (Γ), cut-off energy (E_{cut}) and normalization K_1 and K_2 (one for the PCA spectra and the other for the HXT). Furthermore, in figure 3.8 we show the diagrams of the iron line energy (E_l), and the intensity of the iron line (I_{Fe}) which are the parameters oh the GAUSS model. The iron line width σ was fixed to σ=0.5 kev since it appeared to be narrower than the spectral resolution of the PCA (18% at 6 keV). Finally,figure 3.9 shows the cut-off energy (E_{cut}) as a function of photon index (Γ).

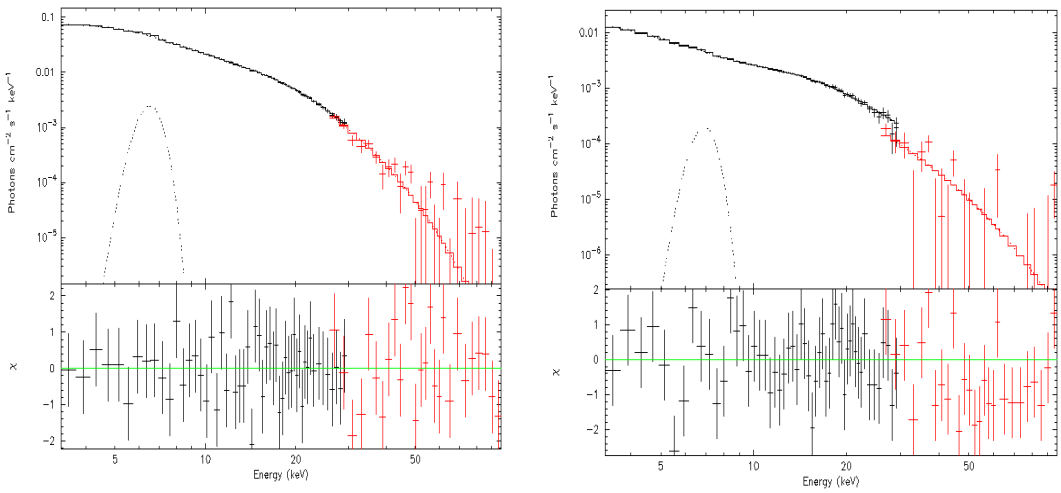

Figure 3.4: Average energy spectra for two different flux levels; Left we see the spectra during the outburst while right at the end of the outburst. Black and red symbols represent PCA and HEXTE data, respectively.

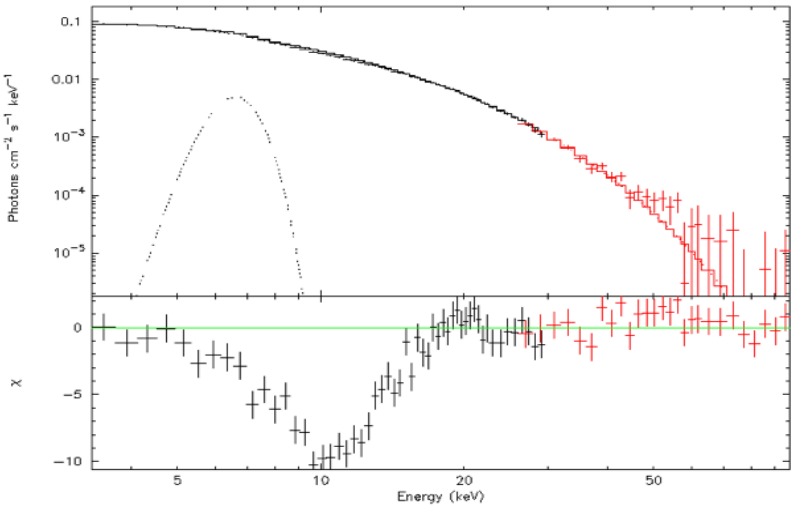

Figure 3.5: The spectral continuum of the source without using the absorption gaussian component.

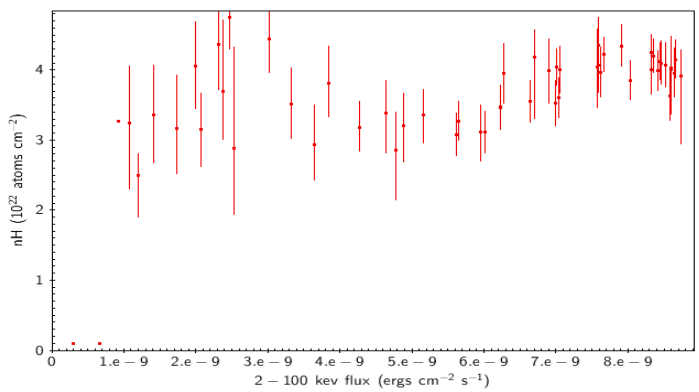

Figure 3.6: The equivalent hydrogen column as a function of X-ray flux.

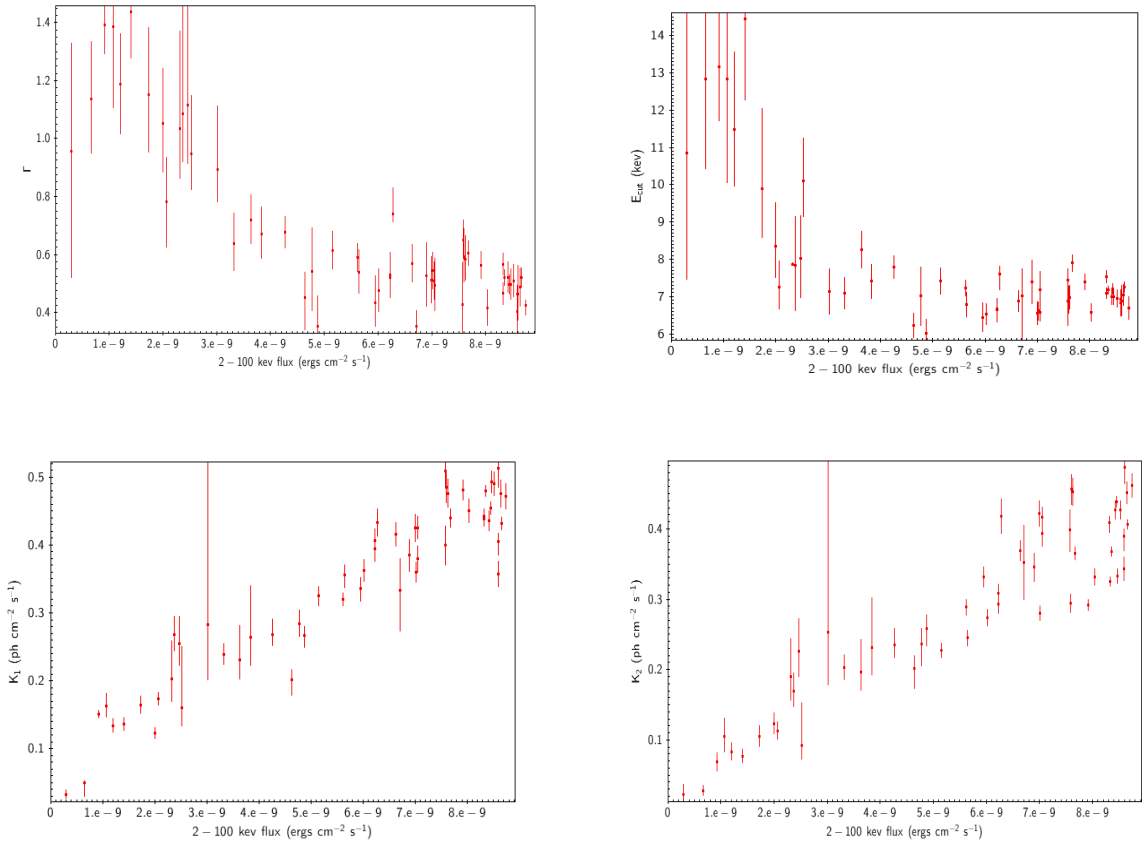

Figure 3.7: Cutoffpl photon index (Γ), cut-off energy (E_{cut}) and normalization (K_1 and K_2) as a function of X-ray flux.

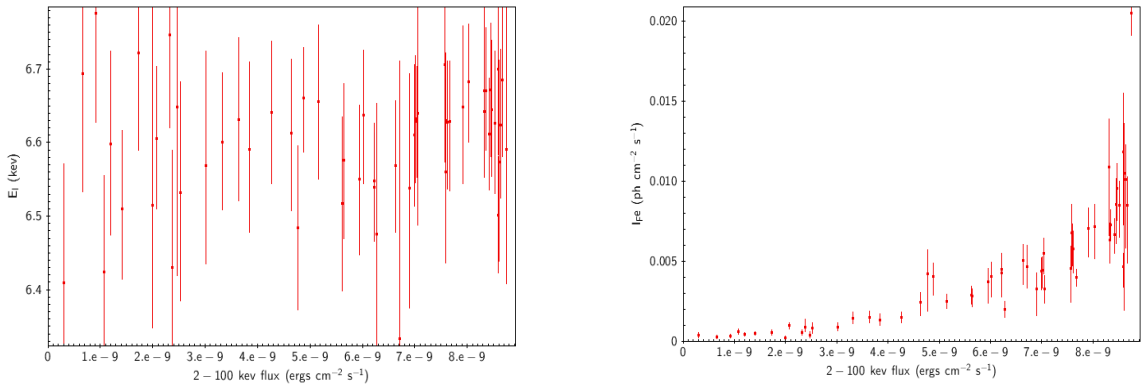

Figure 3.8: The iron line energy E_l and the intensity of the iron line I_{Fe} as a function of X-ray flux.

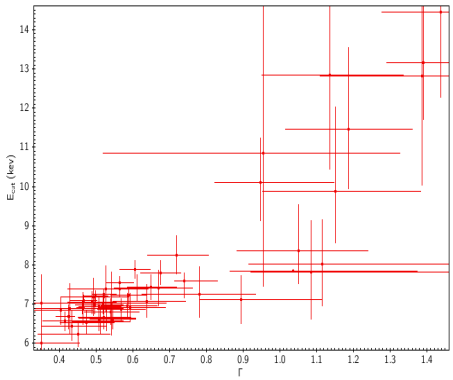

Figure 3.9: The cut-off energy (E_{cut}) as a function of photon index (Γ).

Based on the diagrams we can draw the following conclusions:

- The photon index anticorrelates with X-ray flux. The normalizations K_1 (for the PCA data) and K_2 (for the HXT data) follow the opposite trend.
- Regarding the iron line which is a result of the reprocessing of the hard X-ray continuum in relatively cool matter, we see that centered at 6.4 keV with a small margin. On the other hand, the intensity of the iron line I_{Fe} increase as the X-ray flux increases.
- The cutoff energy approximately follows the same trend as the photon index, namely, it increases as the flux decreases.

3.3 The 10 keV feature.

As we have already mentioned in Chapter 2, there is a deficit of photons at around 10 keV in the spectrum of the 4U1901+03 whose origin is unclear. According to Coburn (2002) this feature affects the X-ray spectral continuum at 8-12 keV. It has been observed in the spectra of many X-ray pulsar, either in emission as in 4U 0115+63 (Ferrigno et al. 2009; Muller et al. 2012) or in absorption such as in XTE J0658–073 (McBride at al. 2006; Nespoli et al. 2012). Muller (2012) shows that in the case of the 4U 0115+634 its energy seems to be slightly anti-correlated with the source flux, while its width remains relatively constant while Nespoli et al (2012) shows that this component is found at almost constant energy.

Figure 3.10 shows the diagrams of the parameters for the 10 keV feature: the central energy of the absorption line (E_0), the width of the absorption line (σ_0) and the line depth (S). The width of the absorption line σ_0 and the line depth S anticorrelates with X-ray while the opposite occurs with the central energy of this absorption line (E_0), which increases as the flux increases.

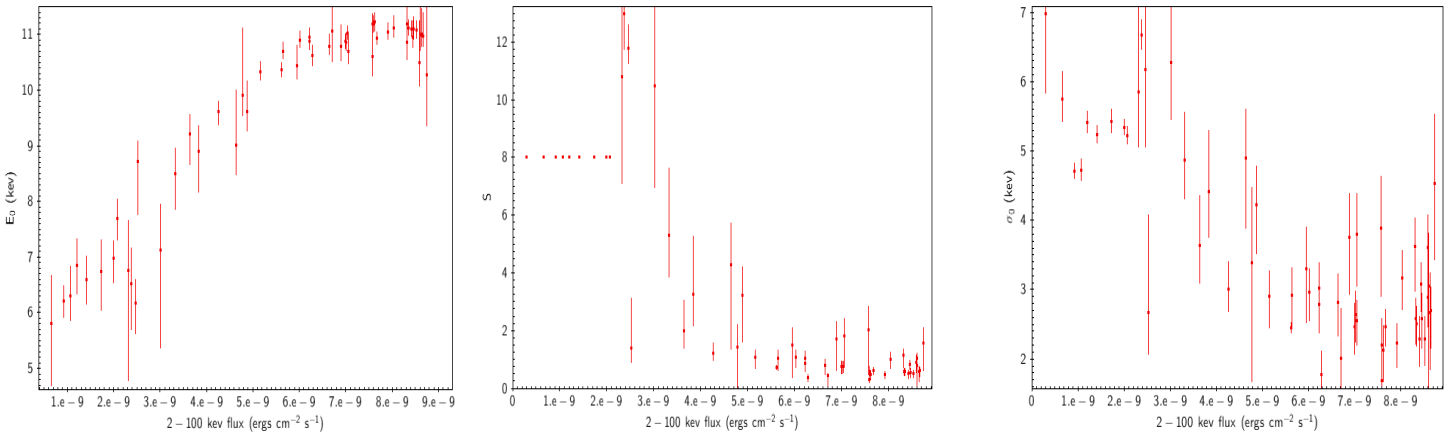

Figure 3.10: The central energy of the absorption line E_0, the width of the absorption line σ_0 and the line depth S as a function of X-ray flux.

3.4 The search for the optical counterpart

An attempt to identify the optical counterpart of 4U 1901+03 was accomplished firstly by using the method described in the study of Reig et al. 2005 which was already discussed in Chapter 2. Figure 3.11 shows the result of this study. At left we see the color-color diagram where stars A, B and C seems to have larger $R - H\alpha$ colors than the other stars and low $B-V$ colors. These stars expected to be early-type stars with large Hα excess and so, according the theory, stars A, B and C appear as potential optical counterparts to 4U1901+03. Right is presented the field around the X-ray position of 4U1901+03 (V-band image). The size of the X-ray error radius of the source reported in this work is ~1′. Unfortunately, we see that none of the candidates stars are inside the cycle which mean that none of them is the optical counterpart of the source.

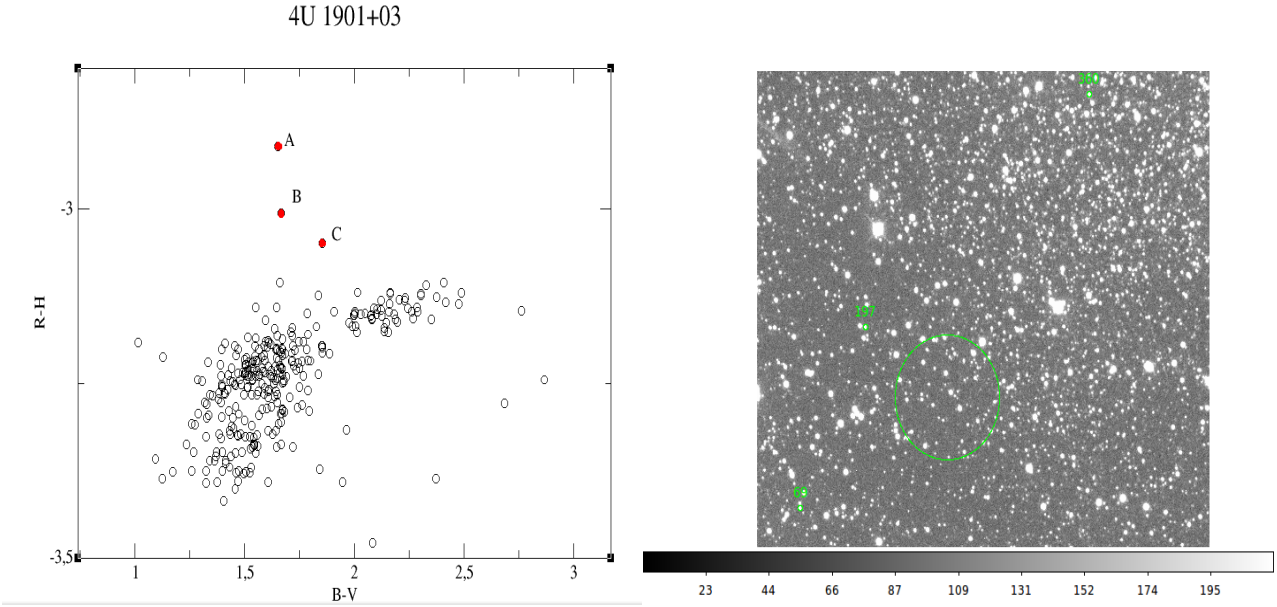

Figure 3.11: Colour-colour diagram and V-band image of the field around 4U 1901 +03. The images were taken from the 1.3m telescope of the Skinakas observatory on 22 July 2015. The radius error circle is shown to the image. The proposed optical counterparts are the A, B and C on the diagrams which corresponds to 360, 197 and 69 respectively.

4U 1901 +03					
Date	MJD	B	V	Ha	R
22-07-15	2457226.4	20.002	18.35	20.2	17.289
22-07-15	2457226.4	20.784	19.117	18.057	21.064
22-07-15	2457226.4	21.613	19.761	21.671	18.621

Table 3.1: Results of the photometric observations for A, B and C stars respectively.

A second attempt to identify the counterpart was made using data from the 2MASS catalog. Negueruela & Scrunch (2007) showed that early-type stars occupy a specific region in the Q-K diagram. Q is defined as

$$Q = (J - H) - 1.70(H - K_S) \quad (3.1)$$

Stars with K_S <12 and Q<0 are possible Be stars. Figure 3.12 shows the Q-K diagram and the image of the field around the X-ray position of 4U1901+03 where the proposed optical counterparts are displayed. Combination of condition 3.1 with Q < 0.0 has been shown to be very efficient at identifying reddened Be stars. Also we choose stars with K_S <12 because magnitudes fainter than K_S =12 would be too reddened to have reliable *J* magnitudes. We find six candidates Be stars (some of them have K_S slightly higher than 12) of which only one (the star with number 900) is inside the X-ray error radius (see table 3.2).

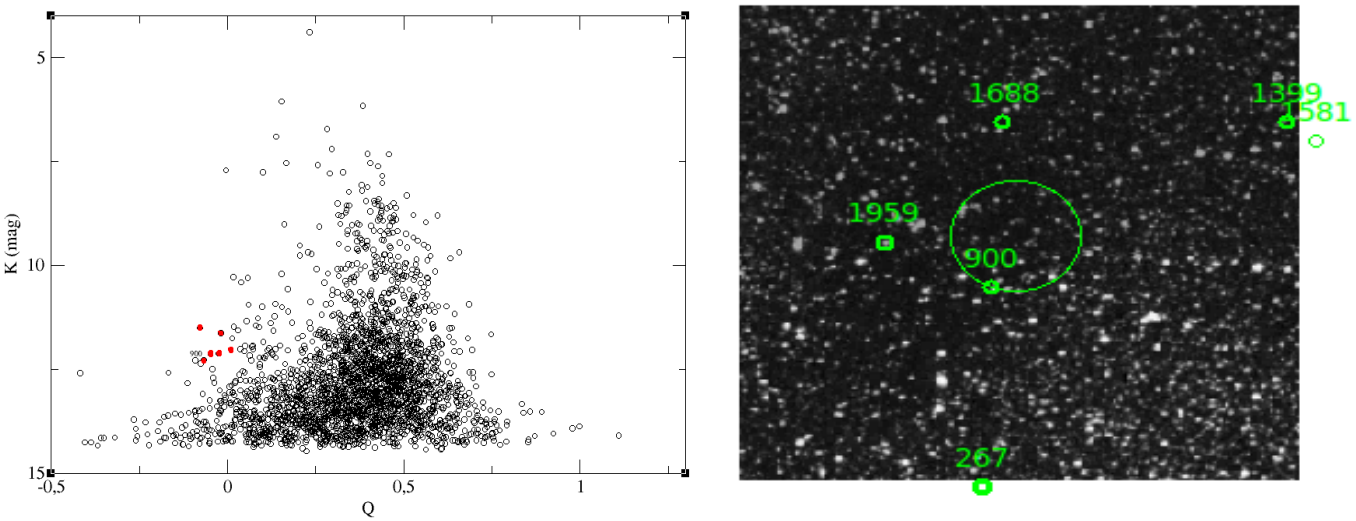

Figure 3.12: At left a plot of IR *Q* values against K_S magnitude for 2MASS stars within 1′ of the position for 4U1901+03. Candidate early-type stars are marked with red color. At right we see the image of the field around 4U 1901 +03 with the candidate Be stars be marked.

ID	Coordinates (RA-DEC)	K_S	Q
267	$19^h\ 03^m39^s.65$-+3°06′14.8"	12.118	-0.025
900	**$19^h\ 03^m39^s.01$-+3°10′30.7"**	**12.275**	**-0.067**
1399	$19^h\ 03^m17^s.42$-+3°14′40.9"	12.012	0.0729
1581	$19^h\ 03^m15^s.33$-+3°13′39.9"	11.67	-0.0156
1688	$19^h\ 03^m38^s.13$-+3°14′50.0"	12.00	0.0086
1959	$19^h\ 03^m46^s.87$-+3°11′28.8"	12.13	-0.048

Table 3.2: Candidate Be stars in the field of 4U 1901+03. Note that only one (number 900) is inside the X-ray error radius

Chapter 4

Discussion

In this thesis we studied the 4U 1901+03 with the aim to

i) Define X-ray spectral states and compare our results with those of Reig and Nespoli (2013).

ii) Study its accretion regimes.

iii) Investigate in detail the "10-keV feature" and discuss whether it can be associated to a cyclotron line.

iv) Identify the optical counterpart.

4.1 Spectral states and accretion regimes

Before we begin to discuss the implications of our work we have to analyze some theory about the processes by which mass is transferred, captured, deposited on the neutron star surface in the form of an accretion column and converted into high-energy radiation. According to Basko & Sunyaev (1976) there exists a critical luminosity, L_{crit}, at which the deceleration of the accreting flow to rest at the neutron star surface occurs by radiation pressure or via Coulomb interactions.

Reig & Nespoli (2013) showed that accreting X-ray binaries with high-mass companions exhibit spectral states in the hardness-intensity diagrams. At low X-ray luminosities the sources populate the horizontal branch (HB), whereas at higher luminosities the sources trace a diagonal branch (DB). For example, figure 4.1 shows the outburst profile and HID of the BeXB KS 1947+300. The two branches are displayed clearly in the HID diagram. When the outburst begins, the system moves rightward on the HID until the luminosity reaches a critical value. Then the source undergoes the transition, and makes a sudden turn in the HID, entering the DB. In this state, as the flux increases, the SC decreases and the system moves leftward on the HID. After the peak luminosity is reached, the hardness starts increasing again, and the system moves back on the DB, tracing the same pattern as during the rise. Reig and Nespoli (2013) proposed that the two branches correspond to two different accretion modes, which depend on a critical value of the luminosity.

For sources that their maximum luminosity is close to the critical luminosity (L_X^{peak} /$L_{crit} \leq 1$) the two branches are not clearly distinguished. The opposite happens when L_X^{peak} /$L_{crit} \geq 7$; In this case, we can see clearly the two branches. Figure 4.2 shows an example of a sub- and super-critical source. Each spectral branch can be associated with one of the two modes of accretion proposed by Becker et al. (2012). The DB, which corresponds to a high-luminosity state, would be associated with the supercritical mode and the HB with the subcritical one. In addition, we can determine the spectral state of a source from the diagrams of the photon index and the cutoff energy with X-ray flux (Reig & Nespoli 2013). More specifically and as we have already mentioned in Chapter

1, the photon index anticorrelates with X-ray flux in the HB and correlates with it in the DB. The cut off energy shows the same behavior.

In 4U1901+03, the DB is not displayed (Fig. 4.3). An attempt to move to that branch can be observed in the diagram of photon index (see Fig. 3.7). Here we see that the photon index firstly anticorrelates with X-ray flux and starts to stay stable as the flux gets larger. That fact leads us to suppose that maybe L_X^{peak} gets very close to L_{crit}. So we can coclude that the case of 4U 1901+03 is similar to XTE J0658-073 (see Fig 4.2); It is a subcritical source in which the maximum luminosity is supposed to get close to its critical luminosity ($L_X^{peak}/L_{crit} \lesssim 1$).

This view is enhanced by the study of Chen et al (2008) about the pulse profiles of the 4U 1901+03. They found a complex variation of the pulse profile which may be related with the radiation mechanism. Specifically, as the flux of the source is high the pulse profile is dominated by the double peak structure. In this case one peak belongs to the fan-beam radiation and the other to the pencil beam radiation. At the end of the outburst the luminosity is reduced to below to $10^{37}\ erg\ s^{-1}$ and the radiation pressure can no longer support the accretion column so the emission escapes from the top of the column, forming a pencil beam. In this case the double peak structure changes to a single peak structure. According to Becker et al (2012) (see Fig. 4.4) there are two different structures (fan and pencil beam) when the source is subcritical with $L_X \lesssim L_{crit}$ (which is our case) while at very low luminosities, the emission occurs via the pencil component only (Burnard et al .1991; Nelson et al. 1993).

We also made the pulse profiles of the source at the beginning and at the end of the outburst; At the beginning of the outburst when the flux of the source is high (February 10) we see clearly two peaks, one for the fan-beam radiation and the other for the pencil beam radiation. For lower flux there is only one peak for the pencil beam as we expected (see Fig. 4.5).

It would be interesting to examine what happen to the source at the end of the outburst when the flux had dropped to below $3.0 \times 10^{-11}\ ergs\ cm^{-2}s^{-1}$. As we see in figure 4.6 pulsations became undetectable. This behavior can be interpreted as the onset of the so-called "propeller effect". This effect is caused when the magnetic field throws the plasma back beyond the capture radius. At the magnetospheric radius where the magnetic pressure equals the plasma pressure, the accreting matter from a disc is "frozen" into the stellar magnetic field lines at a certain distance R_M and rotates with the angular velocity of the star. The matter will fall onto the neutron star only if the its rotational velocity is smaller than the Keplerian velocity at the given distance

$$R_M < R_C = \left(\frac{GM}{\omega^2}\right)^{1/3} = \left(\frac{GMP^2}{4\pi^2}\right)^{1/3}$$

where R_C is the corotation radius M is the neutron star mass and P its rotational period. If we equate the corotation radius to the magnetospheric radius we find the threshold value of accretion luminosity for the onset of the propeller which finally is

$$L_{lim}(R) = \frac{GM\dot{M}_{lim}}{R} \backsimeq 3.9x10^{37}\xi^{\frac{7}{2}}B_{12}^2P_0^{-7/3}M_{1.4}^{-2/3}R_6^5\ erg\ s^{-1} \quad (4.1)$$

where $B_{12}$is the magnetic field strength in units of 10^{12}G, $M_{1.4}$ is the neutron star mass in units of 1.4 $M_\odot\ and\ R_6$ is neutron star radius in units of $10^6 cm$. If the accretion rate decreases below $\dot{M}_{lim}$ accretion is not possible anymore (propeller regime).

According to the relation 4.1 for our source the threshold value of accretion luminosity is $L_{lim} \simeq 10^{36} erg\ s^{-1}$. The lowest luminosity of the source at the end of the outburst is $L_{low} = 3.6{\times}10^{35}\ erg\ s^{-1}$ which is below L_{lim}. Given the fact that pulsations became undetectable at the end of the outburst and that the luminosity of the source at the same time is below the threshold value of accretion luminosity we can assume that the source has entered the "propeller regime" of accretion.

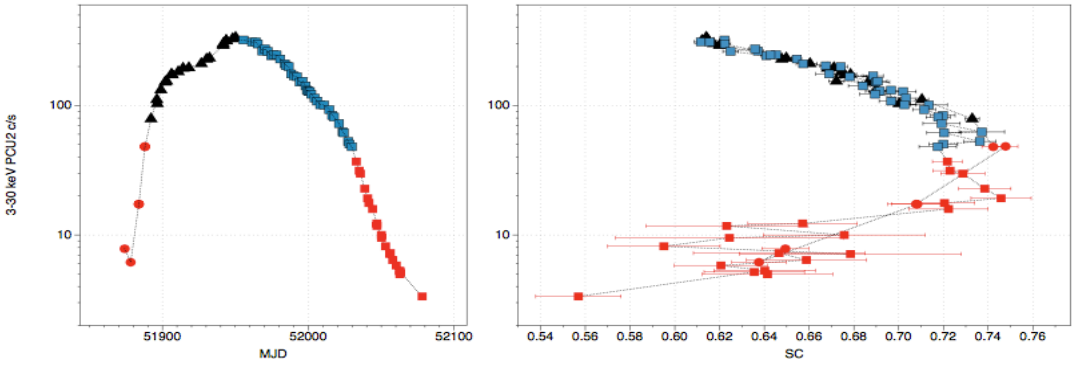

Figure 4.1: Light curve and HID for KS 1947+300.

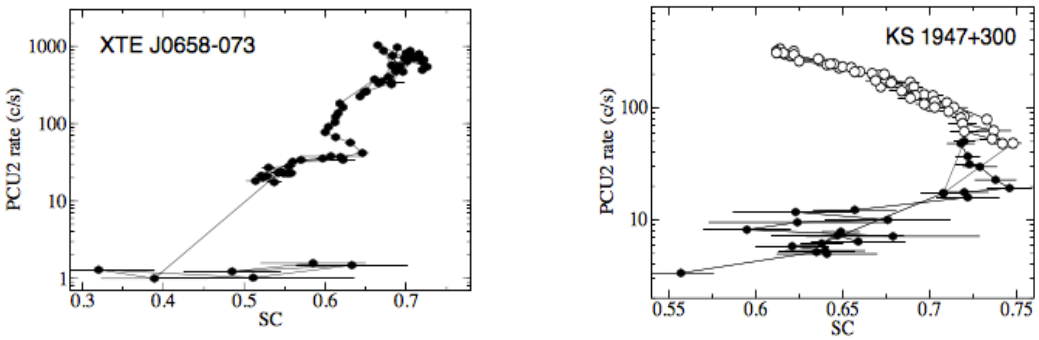

Figure 4.2: Hardness (soft colour)-intensity diagram. The soft colour was defined as the ratio 7-10 keV / 4-7 keV. For the first source (XTE J0658-073) $L_x^{peak}/L_{crit} \leq 1$ while for the second source (KS 1947+300) $L_x^{peak}/L_{crit} \sim 7$.

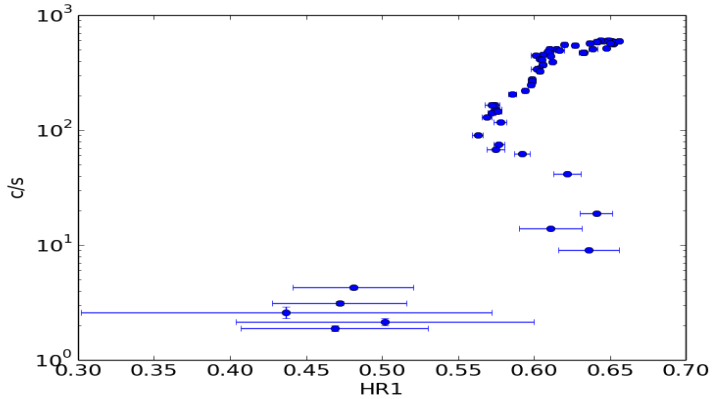

Figure 4.3: The HID diagram of 4U 1901+03

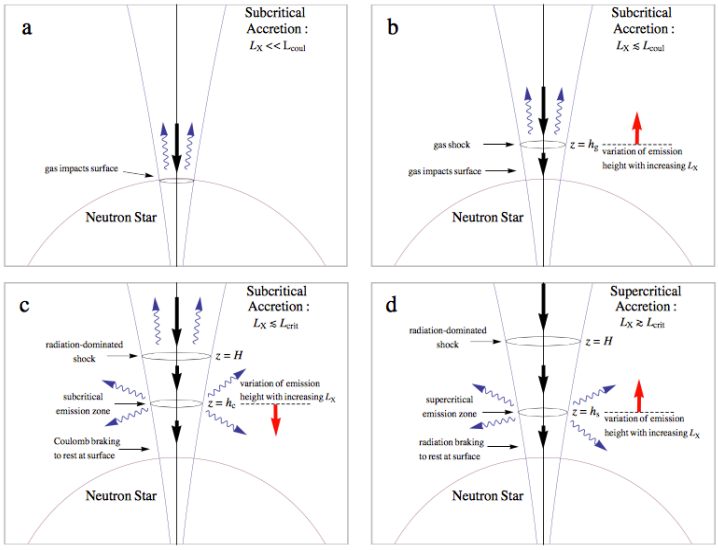

Figure 4.4: Schematic illustration of the geometry of the accretion column (Becker et al 2012).

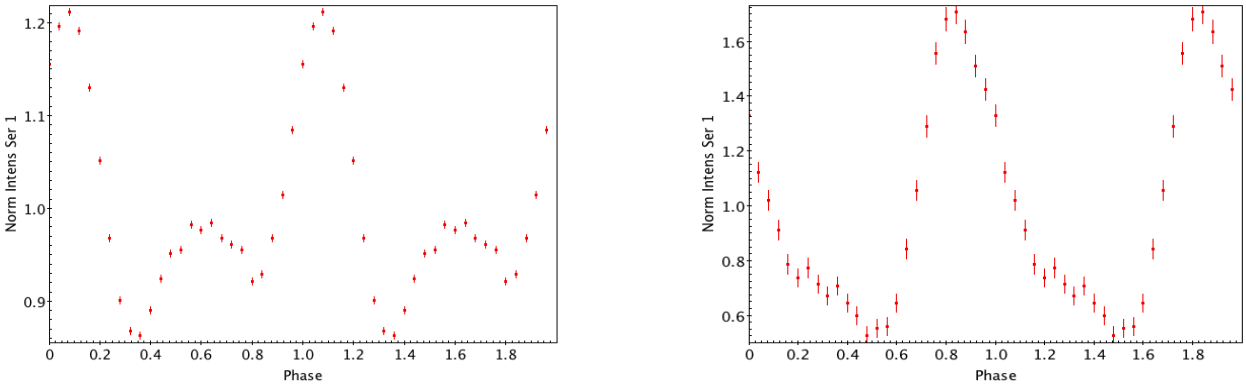

Figure 4.5: Typical pulse profiles at the beginning of the outburst (left) and at the end of the outburst (right).

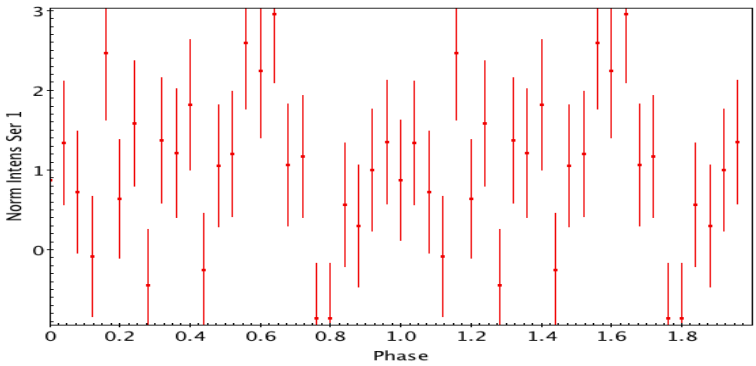

Figure 4.6: Pulse profile of the source at the end of the outburst.

4.2 The 10 kev feature

In this section we investigate whether this feature can be associated with a cyclotron line.

Firstly, we have to perform a test in order to rule out an instrumental origin of the feature. For that reason, we compare the spectrum of 4U1901+03 with that of a non-cyclotron line source like the Crab pulsar. The Crab data were taken the same time period during which the 4U1901+03 were taken. We know that the Crab has no CRSFs, so if this feature were seen in the Crab spectrum we can assume that the 10 kev feature of 4U1901+03 has an instrumental origin.

The model we used for the Crab spectrum was an absorbed powerlaw. We freezed nH at $0.4\text{x}10^{-22}cm^{-2}$ (Weisskopf et al. 2004) and found Γ=2.10 with a normalization of 10.578 photons $\text{ke}V^{-1}cm^{-2}s^{-1}$ at 1kev. As we see in figure 4.7 no absorption-like feature is found at 10 keV in the Crab spectrum and so we can be sure that this feature is not instrumental in origin.

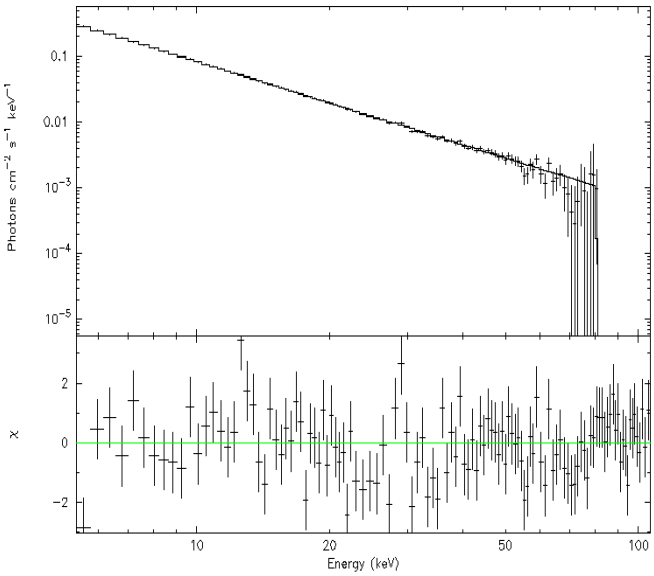

Figure 4.7: The ~4–60 keV spectrum of Crab

After having ruled out the above possibility we will examine this issue from two perspectives:

a) Variability with flux. Given the fact that the 10 keV feature generally stays almost stable in other sources (Nespoli et al 2012) or changes slightly (Muller 2012) we could say that the variability with the flux that the 4U 1901+03 displays is an indication for the association of the 10 keV feature with the cyclotron line.

According to Becker et al (2012) depending on the way that the accretion happens, there is negative or positive correlation between the cyclotron energy and the source luminosity (Becker et al. 2012). Specifically, if a source is dominated by radiation pressure near the stellar surface the CRSF energy is negatively correlated with the source luminosity. On the other hand, if Coulomb interactions decelerate the gas to rest we observe the opposite behavior. In our case the energy of the 10 keV feature

correlates with X-ray flux. According to the above, the positive correlation between the central energy of the absorption feature and X-ray flux would indicate that the source is in the sub-critical regime in agreement with the results from the timing analysis (HID) (see Fig. 4.8).

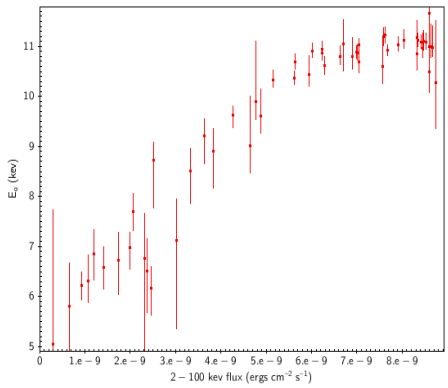

Figure 4.8: The central energy of the absorption line E_0 as a function of X-ray flux.

b) The critical luminosity can be estimated as

$$L_{crit} \approx 1.28\times10^{37}\left(\frac{E_{cyc}}{10kev}\right)^{16/15} erg\ s^{-1}$$

If we consider that the 10 keV feature is a cyclotron line, we find using the above relation that $L_{crit} \approx 1.28\times10^{37}\ erg\ s^{-1}$. As we have already mentioned above we expect the maximum luminosity be close to L_{crit}. Assuming a distance of 10 kpc (Galloway et al 2005) and using the relation

$$L = 4\pi r^2 f$$

we find that the X-ray flux of the source reaches the value of $L_X^{peak}\sim1.1\times10^{38} erg\ s^{-1}$. This is not exactly the result that we would expect. A factor L_X^{peak}/L_{crit} = 8-9 would imply that the source would be in the super-critical regime during a substantial part of the outburst, contrary to the results presented above. At this point its important to mention the uncertainty of the distance that we use to our calculations (10 kpc). Given the fact that no optical counterpart is known and that our calculations is an order-of-magnitude estimated we cannot know the exact distance. So additional calculations using different values for the distance should be made in order to have a complete understanding. At table 4.1 is presented the ratio L_X^{peak}/L_{crit} for three different possible distances. We see that for distance d~5 kpc and d~6 kpc then L_X^{peak}/L_{crit} is ~ 2.6 and ~3.7 respectively. These are not too far from $L_X^{peak}/L_{crit} = \sim 1$ that we find from the HID study, so we believe that this issue could be examine further. Phase resolved spectroscopy from a long observation maybe reveals the origin of this feature.

Distance (kpc)	L_x^{peak} (erg s^{-1})
5	~ 2.6×10^{37}
6	~ 3.7×10^{37}

Table 4.1: The ratio L_X^{peak}/L_{crit} distance 5 and 6 kpc.

4.3 The identification of the optical counterpart

We tried to identify the optical counterpart using two datasets at different wavelengths.

At first we made a colour-colour diagram (the red colour ($R - H\alpha$) as a function of the blue colour ($B - V$)) (see Fig. 3.10) and we found three stars that occupyied the region expected for a Be star. Unfortunately, none of them was in the region of error cycle. An explanation for the lack of a good candidate could be that the optical counterpart is not found because its apparent visual magnitude and color are significantly affected by interstellar extinction in our galaxy.

A second attempt made using datasets from the 2MASS catalog in the near infrared (J (1.25μm), H (1.65μm) and K_S (2.16 μm) bandpasses). The diagram of Q/K_S along with the image of the field around 4U 1901+03 (see Fig. 3.11) showed only one candidate optical counterpart (star number 900). As we see in figure 4.9, this star located at the down and left part of the color-color diagram (B-V=1.371, R-H=-3.348). This is not the result that we expected since Be stars show Hα in emission and so have a larger R-H color.

The discrepancy between the two diagrams may be due to the different dates that the observations were made in the above two cases (22 July 2015 in the first case and between 1997-2001 in the second). One assumption we could make is that firstly (between 1997-2001) the Be star optical counterpart (star number 900) was in an active phase and emission lines observed in the spectra of the star arise from the circumstellar envelope. This situation gradually changed, Be star passed in a non-active phase, the density in the circumstellar envelope became lower and so we could not detect the same star in the last observations we made (at 22 July 2015).

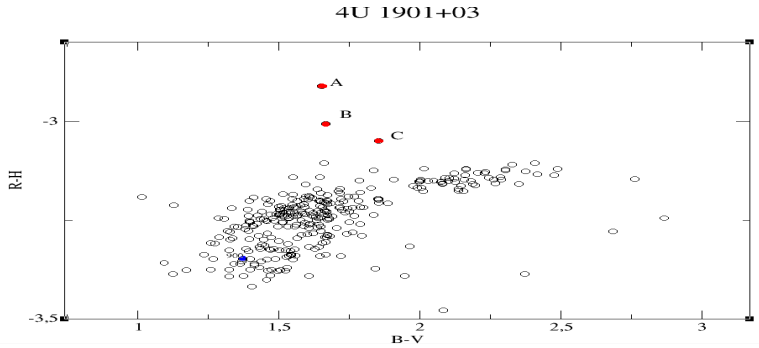

Figure 4.9: Colour-colour diagram. The candidate optical counterpart is marked with blue color. The stars that we expected to be Be stars are marked with red color. None of them are inside the error cycle.

Chapter 5

Conclusions

In this project we have presented a detailed X-ray and optical study of the 4U 1901+03 based on *RXTE* data during the outburst at 2003 and also from Skinakas Observatory at 2015. We studied the accretion regime of the source through timing (hardness-intensity diagram) and spectral analysis.

The presence or not of the two branches (HB and DB) in the HID defines the mode of the accretion and so we have two types of sources: subcritical and supercritical. Our analysis revealed that the 4U 1901+03 is a subcritical source. This conclusion is supported by the fact that only the horizontal branch appears in the HID and by the correlation between the photon index and the cutoff energy with X-ray flux. Also the results from the pulse profiles of the source at the begging and at the end of the outburst enhanced the above theory since at the first case we see two peaks (one for the pencil beam and the other for the fan beam) while for the second we see only one peak (for the pencil beam).The fact that the photon index seems to saturate at very high flux might be an indication that the source reached the critical luminosity.

Taking into consideration that we found the luminosity of the source at the end of the outburst (flux $\sim 3\times10^{-11}\ ergs\ cm^{-2}s^{-1}$) to be below the threshold value of accretion luminosity and the fact that pulsations became undetectable at the same time we have strong evidence that source has entered the "propeller regime" of accretion.

An attempt to identify the origin of the 10 keV feature was also made. Firstly, we excluded an instrumental origin of the feature comparing the spectrum of 4U1901+03 with that of a non-cyclotron line source like the Crab pulsar. Then from the diagram of the energy of the 10 keV feature with the flux we note a positive correlation between them. Taking into consideration that in the most sources which display this feature the energy of the feature stays almost stable with the flux this is maybe an indication that in our case this feature can be associated with a cyclotron line. The fact that the CRSF correlates with flux when a source is subcritical (Becker et al 2012) is in agreement with the results from the timing analysis and so the above statement is corroborated.

From the color-color diagrams (the red colour ($R - H\alpha$) as a function of the blue colour ($B - V$)) and from the Q/K_S diagram (made using data from the 2MASS catalog) we attempt to identify the optical counterpart. Unfortunately, we did not find strong enough evidence that would allow us to conclusively state that we found the true counterpart.

Appendix A

In this chapter we present the best-fit spectral parameters from each observation. NH is the column density, Γ the power law photon index, E_{cut} the cut-off energy, E_0, S and σ_0 the central energy of the absorption line , the line depth of the absorption line and the width of the absorption line, E_l E_{Fe} and σ the iron line energy, the normalization and the iron line width. There is also presented the flux of the source at 2-100 kev and the x^2/N_{dof} where x^2 is the reduced x^2 and N_{dof} is the number of degrees of freedom.

ID	nH(10^22 atoms cm^-2)	Flux at 2-100 kev (erg $cm^{-2}s^{-1}$)	x^2/N_{dof}
70096-01-01-00	$4{,}01^{0.33}_{0.34}$	7.05E-09	0.98/71
70096-01-01-01	$3{,}99^{0.46}_{0.47}$	6.90E-09	0.85/69
70096-01-01-02	$4{,}04^{0.54}_{0.58}$	7.58E-09	1.02/69
70096-01-01-03	$4{,}23^{0.24}_{0.24}$	7.67E-09	0.83/71
70096-01-03-00	$4.01^{0.33}_{0.34}$	8.32E-09	1.12/69
70096-01-03-01G	$4.12^{0.27}_{0.26}$	8.45E-09	1.12/69
70068-22-01-01	$4.25^{0.26}_{0.24}$	8.32E-09	1.07/69
70096-01-03-02	$3.63^{0.35}_{0.35}$	8.59E-09	0.84/69
70068-22-01-02	$4{,}15^{0.29}_{0.26}$	8.66E-09	0.92/69
70096-01-03-03	$3.92^{0.37}_{0.97}$	8.74E-09	1.01/73
70068-22-01-03G	$4{,}01^{0.21}_{0.63}$	8.60E-09	1.49/69
70096-01-03-04	$3.95^{0.36}_{0.33}$	8.64E-09	0.98/69
70096-01-03-05	$4.03^{0.45}_{0.40}$	8.60E-09	0.73/69
70068-22-01-04	$4{,}20^{0.25}_{0.23}$	8.35E-09	1.57/71
70096-01-04-00	$4.34^{0.31}_{0.29}$	7.91E-09	1.12/69
70096-01-04-01	$4.10^{0.32}_{0.30}$	8.47E-09	1.20/69
70096-01-04-02	$4.07^{0.33}_{0.31}$	8.52E-09	1.06/69
70096-01-04-03	$3.85^{0.28}_{0.28}$	8.04E-09	1.47/69
70096-01-04-04	$4.00^{0.29}_{0.28}$	8.42E-09	0.82/69
70096-01-05-00	$4.36^{0.40}_{0.37}$	7.59E-09	0.83/69
70096-01-06-00	$3.97^{0.36}_{0.34}$	7.62E-09	1.07/69
70096-01-06-01	$4.07^{0.39}_{0.38}$	7.59E-09	1.18/69
70096-01-07-00	$4.05^{0.25}_{0.26}$	7.01E-09	0.68/69
70096-01-07-01	$3.61^{0.29}_{0.28}$	7.05E-09	0.80/69
70096-01-08-00	$3.53^{0.33}_{0.32}$	7.00E-09	0.91/69
70096-01-08-01	$4.19^{0.39}_{0.87}$	6.71E-09	0.82/75

70096-01-09-00	$3.55^{0.30}_{0.29}$	6.64E-09	1.01/69
70096-01-09-01	$3.46^{0.31}_{0.30}$	6.23E-09	0.91/69
70096-01-10-00	$3.48^{0.31}_{0.31}$	6.23E-09	1.00/69
70096-01-10-01	$3.96^{0.43}_{0.42}$	6.28E-09	0.92/69
70096-01-11-00	$3.12^{0.30}_{0.29}$	6.02E-09	1.01/69
70096-01-11-01	$3.26^{0.28}_{0.27}$	5.64E-09	1.03/69
70096-01-12-00	$3.11^{0.39}_{0.41}$	5.95E-09	0.89/69
70096-01-12-01	$3.08^{0.31}_{0.30}$	5.62E-09	0.89/71
70096-01-13-00	$3.36^{0.36}_{0.40}$	5.15E-09	0.72/69
70096-01-13-01	$3.20^{0.46}_{0.52}$	4.88E-09	0.69/69
70096-01-13-02	$2.85^{0.54}_{0.71}$	4.78E-09	0.92/69
70096-01-14-00	$3.38^{0.46}_{0.56}$	4.64E-09	0.78/69
70096-01-14-01	$3.18^{0.37}_{0.34}$	4.27E-09	1.03/70
70096-01-15-01	$3.81^{0.53}_{0.48}$	3.84E-09	0.97/70
70096-01-16-00	$2.94^{0.57}_{0.50}$	3.64E-09	1.12/70
70096-01-16-01	$3.51^{0.52}_{0.48}$	3.32E-09	0.95/70
70096-01-17-00	$4.45^{0.70}_{0.48}$	3.02E-09	0.95/70
70096-01-17-01	$2.88^{1.44}_{0.94}$	2.52E-09	1.21/70
70096-01-18-00	$4.76^{0.56}_{0.45}$	2.47E-09	1.15/70
70096-01-18-02	$3.70^{1.02}_{0.69}$	2.38E-09	1.11/70
70096-01-18-01	$4.37^{0.95}_{0.64}$	2.32E-09	0.89/70
70096-01-19-00	$3.16^{0.52}_{0.52}$	2.07E-09	1.34/71
70096-01-19-01	$4.05^{0.63}_{0.60}$	2.00E-09	1.04/71
70096-01-20-00	$3.17^{0.76}_{0.64}$	1.73E-09	0.85/71
70096-01-20-01	$3.37^{0.71}_{0.69}$	1.41E-09	0.80/71
70096-01-21-00	$2.50^{0.31}_{0.59}$	1.20E-09	0.93/71
70096-01-21-01	$3.24^{0.81}_{0.94}$	1.07E-09	0.95/71
70096-01-22-00	$3.27^{0.00}_{0.00}$	9.22E-10	1.06/72
70096-01-22-01	$0.10^{0.00}_{0.00}$	6.61E-10	1.05/72
70096-01-23-00	$0.10^{0.00}_{0.00}$	3.00E-10	0.88/72

ID	Γ	Ecut (kev)	Flux at 2-100 kev (erg $cm^{-2}s^{-1}$)	x^2/N_{dof}
70096-01-01-00	$0.49^{0.09}_{0.09}$	$7.19^{0.48}_{0.48}$	7.05E-09	0.98/71
70096-01-01-01	$0.53^{0.11}_{0.10}$	$7.39^{0.59}_{0.59}$	6.90E-09	0.85/69
70096-01-01-02	$0.43^{0.14}_{0.13}$	$6.88^{0.64}_{0.66}$	7.58E-09	1.02/69
70096-01-01-03	$0.61^{0.04}_{0.04}$	$7.90^{0.22}_{0.22}$	7.67E-09	0.83/71
70096-01-03-00	$0.47^{0.04}_{0.04}$	$7.09^{0.130.}_{0.13}$	8.32E-09	1.12/69
70096-01-03-01G	$0.50^{0.03}_{0.03}$	$7.20^{0.13}_{0.13}$	8.45E-09	1.12/69
70068-22-01-01	$0.57^{0.04}_{0.04}$	$7.54^{0.17}_{0.17}$	8.32E-09	1.07/69
70096-01-03-02	$0.40^{0.09}_{0.09}$	$6.84^{0.34}_{0.35}$	8.59E-09	0.84/69
70068-22-01-02	$0.52^{0.03}_{0.03}$	$7.24^{0.14}_{0.13}$	8.66E-09	0.92/69
70096-01-03-03	$0.43^{0.02}_{0.03}$	$6.68^{0.31}_{0.31}$	8.74E-09	1.01/73
70068-22-01-03G	$0.46^{0.01}_{0.01}$	$6.92^{0.15}_{0.15}$	8.60E-09	1.49/69
70096-01-03-04	$0.49^{0.07}_{0.07}$	$7.04^{0.28}_{0.29}$	8.64E-09	0.98/69
70096-01-03-05	$0.46^{0.10}_{0.09}$	$6.89^{0.41}_{0.40}$	8.60E-09	0.73/69
70068-22-01-04	$0.52^{0.03}_{0.03}$	$7.19^{0.10}_{0.11}$	8.35E-09	1.57/71
70096-01-04-00	$0.56^{0.05}_{0.05}$	$7.38^{0.21}_{0.21}$	7.91E-09	1.12/69
70096-01-04-01	$0.50^{0.05}_{0.05}$	$6.99^{0.22}_{0.22}$	8.47E-09	1.20/69
70096-01-04-02	$0.51^{0.06}_{0.05}$	$6.95^{0.22}_{0.22}$	8.52E-09	1.06/69
70096-01-04-03	$0.42^{0.06}_{0.06}$	$6.57^{0.24}_{0.24}$	8.04E-09	1.47/69
70096-01-04-04	$0.52^{0.06}_{0.05}$	$6.99^{0.22}_{0.22}$	8.42E-09	0.82/69
70096-01-05-00	$0.65^{0.07}_{0.06}$	$7.44^{0.31}_{0.31}$	7.59E-09	0.83/69
70096-01-06-00	$0.59^{0.08}_{0.07}$	$6.96^{0.32}_{0.31}$	7.62E-09	1.07/69
70096-01-06-01	$0.59^{0.10}_{0.09}$	$6.90^{0.37}_{0.36}$	7.59E-09	1.18/69
70096-01-07-00	$0.55^{0.06}_{0.06}$	$6.62^{0.24}_{0.25}$	7.01E-09	0.68/69
70096-01-07-01	$0.51^{0.07}_{0.06}$	$6.57^{0.24}_{0.24}$	7.05E-09	0.80/69
70096-01-08-00	$0.51^{0.08}_{0.08}$	$6.54^{0.30}_{0.30}$	7.00E-09	0.91/69
70096-01-08-01	$0.35^{0.05}_{0.05}$	$7.02^{0.72}_{1.38}$	6.71E-09	0.82/75
70096-01-09-00	$0.57^{0.07}_{0.06}$	$6.87^{0.27}_{0.28}$	6.64E-09	1.01/69
70096-01-09-01	$0.52^{0.07}_{0.07}$	$6.67^{0.28}_{0.28}$	6.23E-09	0.91/69
70096-01-10-00	$0.53^{0.08}_{0.08}$	$6.64^{0.31}_{0.32}$	6.23E-09	1.00/69
70096-01-10-01	$0.74^{0.09}_{0.03}$	$7.59^{0.21}_{0.42}$	6.28E-09	0.92/69
70096-01-11-00	$0.48^{0.08}_{0.07}$	$6.52^{0.29}_{0.29}$	6.02E-09	1.01/69
70096-01-11-01	$0.54^{0.08}_{0.07}$	$6.80^{0.33}_{0.32}$	5.64E-09	1.03/69
70096-01-12-00	$0.43^{0.09}_{0.08}$	$6.44^{0.39}_{0.37}$	5.95E-09	0.89/69
70096-01-12-01	$0.59^{0.05}_{0.05}$	$7.23^{0.21}_{0.22}$	5.62E-09	0.89/71
70096-01-13-00	$0.61^{0.07}_{0.06}$	$7.41^{0.35}_{0.35}$	5.15E-09	0.72/69
70096-01-13-01	$0.35^{0.10}_{0.10}$	$6.01^{0.38}_{0.38}$	4.88E-09	0.69/69
70096-01-13-02	$0.54^{0.15}_{0.14}$	$7.03^{0.78}_{0.81}$	4.78E-09	0.92/69
70096-01-14-00	$0.45^{0.09}_{0.11}$	$6.22^{0.33}_{0.32}$	4.64E-09	0.78/69

70096-01-14-01	$0.68^{0.05}_{0.06}$	$7.79^{0.31}_{0.30}$	4.27E-09	1.03/70
70096-01-15-01	$0.67^{0.09}_{0.08}$	$7.41^{0.45}_{0.46}$	3.84E-09	0.97/70
70096-01-16-00	$0.72^{0.09}_{0.08}$	$8.24^{0.50}_{0.48}$	3.64E-09	1.12/70
70096-01-16-01	$0.64^{0.10}_{0.09}$	$7.08^{0.42}_{0.41}$	3.32E-09	0.95/70
70096-01-17-00	$0.89^{0.22}_{0.11}$	$7.12^{0.61}_{0.61}$	3.02E-09	0.95/70
70096-01-17-01	$0.95^{0.20}_{0.12}$	$10.11^{1.14}_{0.97}$	2.52E-09	1.21/70
70096-01-18-00	$1.12^{0.78}_{0.20}$	$8.03^{1.14}_{1.06}$	2.47E-09	1.15/70
70096-01-18-02	$1.09^{0.40}_{0.16}$	$7.83^{1.30}_{1.21}$	2.38E-09	1.11/70
70096-01-18-01	$1.04^{0.34}_{0.17}$	$7.85^{0.06}_{0.03}$	2.32E-09	0.89/70
70096-01-19-00	$0.78^{0.15}_{0.16}$	$7.26^{0.69}_{0.60}$	2.07E-09	1.34/71
70096-01-19-01	$1.05^{0.19}_{0.17}$	$8.35^{1.17}_{0.83}$	2.00E-09	1.04/71
70096-01-20-00	$1.15^{0.23}_{0.20}$	$9.88^{2.15}_{1.31}$	1.73E-09	0.85/71
70096-01-20-01	$1.44^{0.16}_{0.16}$	$14.45^{3.21}_{2.18}$	1.41E-09	0.80/71
70096-01-21-00	$1.19^{0.17}_{0.17}$	$11.47^{2.08}_{1.51}$	1.20E-09	0.93/71
70096-01-21-01	$1.39^{0.22}_{0.28}$	$12.82^{3.64}_{2.78}$	1.07E-09	0.95/71
70096-01-22-00	$1.39^{0.10}_{0.10}$	$13.16^{1.87}_{1.45}$	9.22E-10	1.06/72
70096-01-22-01	$1.14^{0.20}_{0.18}$	$12.85^{4.21}_{2.40}$	6.61E-10	1.05/72
70096-01-23-00	$0.96^{0.37}_{0.44}$	$10.85^{7.58}_{3.39}$	3.00E-10	0.88/72

ID	E0 (kev)	σ0 (kev)	S	Flux at 2-100 kev (erg $cm^{-2}s^{-1}$)	x^2/N_{dof}
70096-01-01-00	$10.69^{0.30}_{0.21}$	$3.80^{0.59}_{0.74}$	$1.81^{0.59}_{1.02}$	7.05E-09	0.98/71
70096-01-01-01	$10.79^{0.39}_{0.25}$	$3.75^{0.63}_{0.83}$	$1.71^{0.61}_{1.11}$	6.90E-09	0.85/69
70096-01-01-02	$10.60^{0.57}_{0.34}$	$3.88^{0.74}_{0.98}$	$2.03^{0.82}_{1.57}$	7.58E-09	1.02/69
70096-01-01-03	$10.93^{0.11}_{0.11}$	$2.46^{0.26}_{0.28}$	$0.63^{0.11}_{0.14}$	7.67E-09	0.83/71
70096-01-03-00	$10.86^{0.68}_{0.32}$	$3.62^{0.42}_{0.64}$	$1.15^{0.23}_{0.43}$	8.32E-09	1.12/69
70096-01-03-01G	$10.96^{0.30}_{0.19}$	$3.09^{0.30}_{0.39}$	$0.82^{0.13}_{0.19}$	8.45E-09	1.12/69
70068-22-01-01	$11.18^{0.17}_{0.14}$	$2.58^{0.30}_{0.36}$	$0.56^{0.10}_{0.14}$	8.32E-09	1.07/69
70096-01-03-02	$11.67^{0.16}_{0.17}$	$2.89^{0.39}_{0.43}$	$0.90^{0.25}_{0.34}$	8.59E-09	0.84/69
70068-22-01-02	$10.97^{0.43}_{0.19}$	$2.69^{0.33}_{0.54}$	$0.61^{0.11}_{0.20}$	8.66E-09	0.92/69
70096-01-03-03	$10.28^{1.24}_{0.92}$	$4.54^{1.00}_{1.10}$	$1.59^{0.54}_{0.96}$	8.74E-09	1.01/73
70068-22-01-03G	$10.50^{0.76}_{0.42}$	$3.60^{0.47}_{0.62}$	$1.05^{0.18}_{0.35}$	8.60E-09	1.49/69
70096-01-03-04	$11.00^{0.45}_{0.21}$	$2.67^{0.57}_{0.82}$	$0.57^{0.19}_{0.34}$	8.64E-09	0.98/69
70096-01-03-05	$11.00^{1.05}_{0.28}$	$3.05^{0.76}_{1.47}$	$0.80^{0.33}_{0.93}$	8.60E-09	0.73/69
70068-22-01-04	$11.12^{0.14}_{0.12}$	$2.52^{0.25}_{0.32}$	$0.58^{0.10}_{0.15}$	8.35E-09	1.57/71
70096-01-04-00	$11.04^{0.16}_{0.13}$	$2.23^{0.28}_{0.35}$	$0.49^{0.09}_{0.13}$	7.91E-09	1.12/69
70096-01-04-01	$11.10^{0.22}_{0.18}$	$2.58^{0.37}_{0.42}$	$0.53^{0.13}_{0.17}$	8.47E-09	1.20/69
70096-01-04-02	$11.09^{0.17}_{0.15}$	$2.30^{0.32}_{0.39}$	$0.52^{0.11}_{0.15}$	8.52E-09	1.06/69

70096-01-04-03	$11.11^{0.22}_{0.16}$	$3.16^{0.39}_{0.46}$	$0.99^{0.24}_{0.33}$	8.04E-09	1.47/69
70096-01-04-04	$11.09^{0.14}_{0.13}$	$2.30^{0.32}_{0.39}$	$0.52^{0.11}_{0.16}$	8.42E-09	0.82/69
70096-01-05-00	$11.19^{0.19}_{0.19}$	$1.68^{0.31}_{0.40}$	$0.29^{0.09}_{0.12}$	7.59E-09	0.83/69
70096-01-06-00	$11.23^{0.17}_{0.17}$	$2.13^{0.35}_{0.45}$	$0.46^{0.13}_{0.19}$	7.62E-09	1.07/69
70096-01-06-01	$11.19^{0.15}_{0.15}$	$2.20^{0.39}_{0.47}$	$0.57^{0.16}_{0.25}$	7.59E-09	1.18/69
70096-01-07-00	$10.86^{0.17}_{0.14}$	$2.64^{0.34}_{0.40}$	$0.75^{0.17}_{0.24}$	7.01E-09	0.68/69
70096-01-07-01	$11.03^{0.13}_{0.12}$	$2.55^{0.30}_{0.36}$	$0.77^{0.16}_{0.22}$	7.05E-09	0.80/69
70096-01-08-00	$10.89^{0.13}_{0.12}$	$2.46^{0.33}_{0.39}$	$0.77^{0.18}_{0.26}$	7.00E-09	0.91/69
70096-01-08-01	$11.06^{0.48}_{0.55}$	$2.01^{0.71}_{0.71}$	$0.45^{0.08}_{0.82}$	6.71E-09	0.82/75
70096-01-09-00	$10.80^{0.21}_{0.15}$	$2.82^{0.41}_{0.48}$	$0.81^{0.21}_{0.30}$	6.64E-09	1.01/69
70096-01-09-01	$10.88^{0.19}_{0.14}$	$2.78^{0.34}_{0.41}$	$0.87^{0.20}_{0.28}$	6.23E-09	0.91/69
70096-01-10-00	$10.95^{0.16}_{0.15}$	$3.02^{0.37}_{0.42}$	$1.03^{0.26}_{0.36}$	6.23E-09	1.00/69
70096-01-10-01	$10.63^{0.18}_{0.18}$	$1.78^{0.34}_{0.39}$	$0.39^{0.11}_{0.15}$	6.28E-09	0.92/69
70096-01-11-00	$10.90^{0.17}_{0.13}$	$2.96^{0.34}_{0.41}$	$1.09^{0.25}_{0.35}$	6.02E-09	1.01/69
70096-01-11-01	$10.69^{0.16}_{0.14}$	$2.91^{0.40}_{0.46}$	$1.06^{0.29}_{0.42}$	5.64E-09	1.03/69
70096-01-12-00	$10.44^{0.37}_{0.24}$	$3.31^{0.60}_{0.77}$	$1.49^{0.61}_{1.11}$	5.95E-09	0.89/69
70096-01-12-01	$10.36^{0.14}_{0.13}$	$2.45^{0.07}_{0.07}$	$0.74^{0.06}_{0.06}$	5.62E-09	0.89/71
70096-01-13-00	$10.32^{0.19}_{0.14}$	$2.91^{0.37}_{0.46}$	$1.06^{0.25}_{0.38}$	5.15E-09	0.72/69
70096-01-13-01	$9.61^{0.55}_{0.34}$	$4.23^{0.55}_{0.71}$	$3.23^{0.97}_{1.63}$	4.88E-09	0.69/69
70096-01-13-02	$9.90^{1.20}_{0.37}$	$3.39^{1.08}_{1.71}$	$1.43^{0.78}_{2.48}$	4.78E-09	0.92/69
70096-01-14-00	$9.02^{0.99}_{0.54}$	$4.90^{0.71}_{1.01}$	$4.30^{1.43}_{2.92}$	4.64E-09	0.78/69
70096-01-14-01	$9.62^{0.19}_{0.25}$	$3.00^{0.40}_{0.32}$	$1.21^{0.36}_{0.25}$	4.27E-09	1.03/70
70096-01-15-01	$8.90^{0.45}_{0.73}$	$4.42^{0.88}_{0.66}$	$3.27^{2.02}_{1.08}$	3.84E-09	0.97/70
70096-01-16-00	$9.21^{0.34}_{0.55}$	$3.64^{0.72}_{0.55}$	$1.98^{1.07}_{0.60}$	3.64E-09	1.12/70
70096-01-16-01	$8.51^{0.45}_{0.45}$	$4.86^{0.69}_{0.55}$	$5.29^{2.33}_{1.44}$	3.32E-09	0.95/70
70096-01-17-00	$7.12^{0.82}_{1.76}$	$6.27^{1.42}_{0.81}$	$10.50^{9.00}_{3.52}$	3.02E-09	0.95/70
70096-01-17-01	$8.72^{0.37}_{0.95}$	$2.67^{1.41}_{0.61}$	$1.41^{1.72}_{0.51}$	2.52E-09	1.21/70
70096-01-18-00	$6.17^{0.43}_{0.54}$	$6.17^{3.12}_{1.11}$	$11.79^{0.83}_{0.54}$	2.47E-09	1.15/70
70096-01-18-02	$6.51^{0.64}_{0.83}$	$6.68^{0.22}_{0.21}$	$13.00^{1.26}_{1.23}$	2.38E-09	1.11/70
70096-01-18-01	$6.77^{0.89}_{1.98}$	$5.85^{1.43}_{0.80}$	$10.80^{10.15}_{3.70}$	2.32E-09	0.89/70
70096-01-19-00	$7.69^{0.35}_{0.38}$	$5.22^{0.12}_{0.12}$	$8.00^{0.00}_{0.00}$	2.07E-09	1.34/71
70096-01-19-01	$6.98^{0.30}_{0.44}$	$5.34^{0.12}_{0.11}$	$8.00^{0.00}_{0.00}$	2.00E-09	1.04/71
70096-01-20-00	$6.73^{0.56}_{0.69}$	$5.43^{0.18}_{0.16}$	$8.00^{0.00}_{0.00}$	1.73E-09	0.85/71
70096-01-20-01	$6.59^{0.42}_{0.44}$	$5.24^{0.13}_{0.12}$	$8.00^{0.00}_{0.00}$	1.41E-09	0.80/71
70096-01-21-00	$6.86^{0.48}_{0.51}$	$5.41^{0.15}_{0.14}$	$8.00^{0.00}_{0.00}$	1.20E-09	0.93/71
70096-01-21-01	$6.31^{0.53}_{0.44}$	$4.72^{0.16}_{0.15}$	$8.00^{0.00}_{0.00}$	1.07E-09	0.95/71
70096-01-22-00	$6.22^{0.28}_{0.29}$	$4.71^{0.12}_{0.11}$	$8.00^{0.00}_{0.00}$	9.22E-10	1.06/72
70096-01-22-01	$5.80^{0.86}_{1.11}$	$5.75^{0.39}_{0.32}$	$8.00^{0.00}_{0.00}$	6.61E-10	1.05/72
70096-01-23-00	$5.05^{2.68}_{4.97}$	$6.98^{2.02}_{1.14}$	$8.00^{0.00}_{0.00}$	3.00E-10	0.88/72

ID	El (kev)	I_{Fe} (photons $cm^{-2}s^{-1}$)	Flux at 2-100 kev (erg $cm^{-2}s^{-1}$)	x^2/N_{dof}
70096-01-01-00	$6.639^{0.146}_{0.152}$	$0.003^{0.001}_{0.001}$	7.05E-09	0.98/71
70096-01-01-01	$6.539^{0.155}_{0.164}$	$0.003^{0.001}_{0.002}$	6.90E-09	0.85/69
70096-01-01-02	$6.707^{0.127}_{0.133}$	$0.005^{0.001}_{0.002}$	7.58E-09	1.02/69
70096-01-01-03	$6.629^{0.082}_{0.095}$	$0.004^{0.001}_{0.001}$	7.67E-09	0.83/71
70096-01-03-00	$6.670^{0.131}_{0.117}$	$0.011^{0.003}_{0.004}$	8.32E-09	1.12/69
70096-01-03-01G	$6.672^{0.090}_{0.090}$	$0.009^{0.002}_{0.002}$	8.45E-09	1.12/69
70068-22-01-01	$6.642^{0.083}_{0.083}$	$0.006^{0.001}_{0.001}$	8.32E-09	1.07/69
70096-01-03-02	$6.501^{0.079}_{0.078}$	$0.005^{0.001}_{0.001}$	8.59E-09	0.84/69
70068-22-01-02	$6.686^{0.103}_{0.104}$	$0.009^{0.002}_{0.004}$	8.66E-09	0.92/69
70096-01-03-03	$6.591^{0.271}_{0.183}$	$0.021^{0.001}_{0.001}$	8.74E-09	1.01/73
70068-22-01-03G	$6.700^{0.118}_{0.117}$	$0.012^{0.004}_{0.005}$	8.60E-09	1.49/69
70096-01-03-04	$6.624^{0.104}_{0.100}$	$0.010^{0.002}_{0.004}$	8.64E-09	0.98/69
70096-01-03-05	$6.574^{0.139}_{0.135}$	$0.010^{0.003}_{0.009}$	8.60E-09	0.73/69
70068-22-01-04	$6.671^{0.086}_{0.081}$	$0.007^{0.001}_{0.001}$	8.35E-09	1.57/71
70096-01-04-00	$6.649^{0.110}_{0.104}$	$0.007^{0.001}_{0.002}$	7.91E-09	1.12/69
70096-01-04-01	$6.645^{0.095}_{0.091}$	$0.010^{0.002}_{0.002}$	8.47E-09	1.20/69
70096-01-04-02	$6.626^{0.098}_{0.096}$	$0.008^{0.002}_{0.002}$	8.52E-09	1.06/69
70096-01-04-03	$6.683^{0.078}_{0.082}$	$0.007^{0.001}_{0.002}$	8.04E-09	1.47/69
70096-01-04-04	$6.611^{0.075}_{0.076}$	$0.007^{0.001}_{0.001}$	8.42E-09	0.82/69
70096-01-05-00	$6.560^{0.126}_{0.124}$	$0.007^{0.002}_{0.002}$	7.59E-09	0.83/69
70096-01-06-00	$6.628^{0.083}_{0.091}$	$0.006^{0.001}_{0.001}$	7.62E-09	1.07/69
70096-01-06-01	$6.630^{0.092}_{0.090}$	$0.006^{0.001}_{0.00}$	7.59E-09	1.18/69
70096-01-07-00	$6.632^{0.085}_{0.087}$	$0.004^{0.001}_{0.001}$	7.01E-09	0.68/69
70096-01-07-01	$6.629^{0.075}_{0.076}$	$0.006^{0.001}_{0.001}$	7.05E-09	0.80/69
70096-01-08-00	$6.610^{0.096}_{0.097}$	$0.004^{0.001}_{0.001}$	7.00E-09	0.91/69
70096-01-08-01	$6.333^{0.377}_{0.413}$	$0.005^{0.001}_{0.001}$	6.71E-09	0.82/75
70096-01-09-00	$6.569^{0.089}_{0.091}$	$0.005^{0.001}_{0.001}$	6.64E-09	1.01/69
70096-01-09-01	$6.548^{0.078}_{0.082}$	$0.004^{0.001}_{0.002}$	6.23E-09	0.91/69
70096-01-10-00	$6.539^{0.074}_{0.073}$	$0.004^{0.001}_{0.001}$	6.23E-09	1.00/69
70096-01-10-01	$6.475^{0.178}_{0.197}$	$0.002^{0.001}_{0.001}$	6.28E-09	0.92/69
70096-01-11-00	$6.637^{0.089}_{0.093}$	$0.004^{0.001}_{0.001}$	6.02E-09	1.01/69
70096-01-11-01	$6.577^{0.104}_{0.107}$	$0.003^{0.001}_{0.001}$	5.64E-09	1.03/69
70096-01-12-00	$6.550^{0.101}_{0.102}$	$0.004^{0.001}_{0.001}$	5.95E-09	0.89/69
70096-01-12-01	$6.518^{0.118}_{0.120}$	$0.003^{0.001}_{0.001}$	5.62E-09	0.89/71
70096-01-13-00	$6.656^{0.104}_{0.105}$	$0.002^{0.000}_{0.000}$	5.15E-09	0.72/69
70096-01-13-01	$6.661^{0.069}_{0.073}$	$0.004^{0.001}_{0.001}$	4.88E-09	0.69/69
70096-01-13-02	$6.484^{0.111}_{0.112}$	$0.004^{0.001}_{0.002}$	4.78E-09	0.92/69

70096-01-14-00	$6.613^{0.100}_{0.105}$	$0.002^{0.001}_{0.001}$	4.64E-09	0.78/69
70096-01-14-01	$6.641^{0.096}_{0.097}$	$0.002^{0.000}_{0.000}$	4.27E-09	1.03/70
70096-01-15-01	$6.591^{0.119}_{0.113}$	$0.001^{0.000}_{0.000}$	3.84E-09	0.97/70
70096-01-16-00	$6.632^{0.112}_{0.110}$	$0.001^{0.000}_{0.000}$	3.64E-09	1.12/70
70096-01-16-01	$6.601^{0.095}_{0.092}$	$0.001^{0.000}_{0.000}$	3.32E-09	0.95/70
70096-01-17-00	$6.569^{0.156}_{0.134}$	$0.001^{0.000}_{0.000}$	3.02E-09	0.95/70
70096-01-17-01	$6.532^{0.151}_{0.147}$	$0.001^{0.000}_{0.000}$	2.52E-09	1.21/70
70096-01-18-00	$6.649^{0.355}_{0.229}$	$0.000^{0.000}_{0.000}$	2.47E-09	1.15/70
70096-01-18-02	$6.430^{0.160}_{0.145}$	$0.001^{0.000}_{0.000}$	2.38E-09	1.11/70
70096-01-18-01	$6.746^{0.141}_{0.127}$	$0.001^{0.000}_{0.000}$	2.32E-09	0.89/70
70096-01-19-00	$6.606^{0.098}_{0.095}$	$0.001^{0.000}_{0.000}$	2.07E-09	1.34/71
70096-01-19-01	$6.514^{0.270}_{0.167}$	$0.000^{0.000}_{0.000}$	2.00E-09	1.04/71
70096-01-20-00	$6.722^{0.142}_{0.133}$	$0.001^{0.000}_{0.000}$	1.73E-09	0.85/71
70096-01-20-01	$6.510^{0.106}_{0.096}$	$0.000^{0.000}_{0.000}$	1.41E-09	0.80/71
70096-01-21-00	$6.598^{0.126}_{0.124}$	$0.000^{0.000}_{0.000}$	1.20E-09	0.93/71
70096-01-21-01	$6.424^{0.131}_{0.128}$	$0.001^{0.000}_{0.000}$	1.07E-09	0.95/71
70096-01-22-00	$6.776^{0.159}_{0.149}$	$0.000^{0.000}_{0.000}$	9.22E-10	1.06/72
70096-01-22-01	$6.693^{0.164}_{0.160}$	$0.000^{0.000}_{0.000}$	6.61E-10	1.05/72
70096-01-23-00	$6.409^{0.162}_{0.157}$	$0.000^{0.000}_{0.000}$	3.00E-10	0.88/72

Bibliography

1. Balucinska-Church, M., & McCammon, D, Photoelectric absorption cross sections with variable abundances, ApJ 400, 699 (1992)

2. Basko, M. M. & Sunyaev, R. A., The limiting luminosity of accreting neutron stars with magnetic fields, MNRAS 175, 395 (1976)

3. Becker, P.A., Klochkov, D., Schonherr, G., Nishimura, O. Ferrigno, C. et al., Spectral Formation in Accreting X-Ray Pulsars: Bimodal Variation of the Cyclotron Energy with Luminosity, A&A 544, A123 (2012)

4. Bilicki,M., Jarrett, T.,Peacock, J. , Cluver, M. , & Steward, L., 2MASS Photometric Redshift catalog: a comprehensive three-dimensional census of the whole sky, ApJS, 210, 9 (2013)

5. Bozzo, E., Romano, P., Ducci, L., Bernardini, F., & Falanga, M., Supergiant fast X-ray transients as an under-luminous class of supergiant X-ray binaries, arXiV:1411.4470B (2014)

6. Bradt, H., Swank, J., & Rothschild, R., X-Ray Timing Explorer Mission, A&AS 97,355 (1993)

7. Burnard, David J., Arons, J., Richard, & Klein, I., Accretion powered pulsars - Continuum spectra and light curves of settling accretion mounds, ApJ 367, 575B (1991)

8. Campana, S., Stella, L., Israel G. L., Moretti, A., Parmar A. N., & Orlandini M., The Quiescent X-Ray Emission of Three Transient X-Ray Pulsars, ApJ 580, 389 (2002)

9. Čechura, J.,Hadrava, & P., Stellar wind in state transitions of high-mass X-ray binaries, A&A 575, A5 (2015)

10. Charles,P.A., & Coe, M.J., Optical, Ultraviolet and Infrared Observations of X-ray Binaries, arxiv:astro-ph/0308020v2 (2003)

11. Chaty, S., An INTEGRAL view of High Mass X-ray Binaries : their nature, formation and evolution, Proceedings of Science , arXiV:1302.4195v1 (2013)

12. Chen, W., Qu, J.-L., Zhang, S., Zhang, F., & Zhang, G.B., A Study on the Pulse Profiles of the HMXB 4U 1901+03, Chinese Astronomy and Astrophysics 32, 241 (2008)

13. Coburn, W., Heindl, W. A., Rothschild, R. E., Gruber, D. E., Kreykenbohm, I., Wilms, J., Kretschmar, P., & Staubert, R., Magnetic Fields of Accreting X-Ray Pulsars with the Rossi X-Ray Timing Explorer, ApJ 580, 394 (2002)

14. Cohen, D. H., Hanson, M. M., Townsend, R. H. D., Bjork- man, K. S., & Gage, M., Diagnostics of Disks Around Hot Stars, ASP Conference Series 337, 59 (2005)

15. Collins, George W., & Truax, Ryland J., Classical rotational broadening of spectral lines, ApJ 439, 860 (1995)

16. DeCesar ME, Boyd PT, Pottschmidt K, Wilms J, Suchy S, Miller M.,C., The Be X- Ray Binary Swift J1626.6−5156 as a Variable Cyclotron Line Source, ApJ 762,61 (2013)

17. Ducci, L., Doroshenko,V., Romano,P., Santangel, A., & Sasaki, M., Expected number of supergiant fast X-ray transients in the Milky Way, Astrophysics and Space Science, 568 A76 (2014)

18. Ebisawa , K., Ueda, Y., Inoue, H., Tanaka, Y., White, & Nicholas, E., ASCA Observations of the Iron Line Structure in Cygnus X-1, ApJ 467, 419E (1996)

19. Edgar, R.G., A Review of Bondi--Hoyle--Lyttleton Accretion , New Astron.Rev. 48, 843 (2004)

20. Ferrigno, C., Becker, P. A., Segreto, A., Mineo, T., & Santangelo, A., Study of the accreting pulsar 4U 0115+634 with a bulk and thermal Comptonization model, A&A, 498, 825

21. Forman, W., Tananbaum, H., & Jones, C. , UHURU observations of the galactic plane in 1970, 1971, and 1972, ApJ 206, L29 (1976)

22. Frank, J., King, A., & Raine, D., Accretion Power in Astrophysics, Cambridge University Press: Cambridge, UK. (2002)
Galloway, D. K., Remillard, R., & Morgan, E., X1901+031, IAU Circ., 8081, 2 (2003a)

23. Frank, J., King A., & Raine,D., Accretion Power in Astrophysics, Cambringe University Press (2002)

24. Galloway, D. K., Remillard, R. A., Morgan, E. H., & Swank, J., X1901+031, IAU Circ., 8070 (2003b)

25. Galloway, D. K., Wang, Z., & Morgan, E. H. , Discovery of pulsations in the X-ray transient 4U 1901+03, ApJ 635, 1217 (2005)

26. Gehrz, R. D., Hackwell, J. A., & Jones, T. W, Circumstellar dust emission from WC9 stars, Astrophysical Journal 194, 619 (1974)

27. Hanuschik, R.W., On the structure of Be star disks, A&A 308, 170 (1996)

28. Hayasaki, K. & Ozakaki, A.T., Accretion disc formation around the neutron star in Be/X-ray binaries, MNRAS 350, 971 (2004)

29. Indebetouw, R., Mathis, J. S.; Babler, B. L.; Meade, M. R.; Watson, C.; Whitney, B. A.; Wolff, M. J.;, et al., The Wavelength Dependence of Interstellar Extinction from 1.25 to 8.0 μm Using GLIMPSE Data, ApJ 619, 931 (2005)

30. Jahoda, K., Swank, J. H., Giles, A. B., Stark, M. J., Strohmayer, T., Zhang, W., & Morgan, E. H., In-orbit performance and calibration of the Rossi X-ray Timing Explorer (RXTE) Proportional Counter Array (PCA), Proc. SPIE 2808, 59 (1996)

31. James M., Paul B., Devasia J., & Indulekha K., Flares, Broadening of the Pulse frequency peak, and Quasi Periodic Oscillations in the Transient X-ray Pulsar 4U 1901+03 arXiv:1008.2815v1 (2010)

32. Kretschmar,P., Nespoli,E., Reig, P., & Anders, F., The Be X-ray Binary Outburst Zoo, arXiv:1302.3434 (2013)

33. Kriss, G. A., Cioffi, D. F., & Canizares, C. R. The X-ray emitting gas in poor clusters with central dominant galaxies, ApJ 272, 439 (1983)

34. Kudritzki R.P., & Puls, J., Winds from Hot Stars, ARAA 38, 613 (2000)

35. La Palombara, N., Sidoli, L., Esposito, P., Tiengo, A., & Mereghetti, S., XMM-Newton observation of the persistent Be/N S X-ray binary pulsar RX J1037.5-5647 in a low luminosity state, A&A 505, 947 (2009)

36. Lei Y.-J., Chen W., Qu J.-L., Song L.-M., Zhang S., Lu Y.,Zhang H.T., & Li T.P., Phase-resolved spectral analysis of 4U 1901+03 during its outburst, Astroph. J. 707, 1016 (2009)

37. Liedahl, D.A., Resonant Auger Destruction and Iron K-Alpha Spectra in Compact X-ray Sources, arXiv:astro-ph/0502002 (2005)

38. Marykutty, J., Biswajit, P., Jincy, D & Kavila, I., Flares, Broadening of the Pulse frequency peak, and Quasi Periodic Oscillations in the Transient X-ray Pulsar 4U 1901+03, MNRAS 410, 1489 (2011)

39. McBride, V. A., Coburn, W., Coe, M. J., Kretschmar, P., Kreykenbohm, I., & Rothschild, R., Phase resolved study of the CRSF in MX 0656-072, Advances in Space Research 38, 2768 (2006)

40. Molkov, S., Lutovinov, A., & Grebenev, S., First results from TOO observations of the Aql X-1 field with INTEGRAL, A&A 411, L357 (2003)

41. Motch, C., Stella, L., Janot-Pacheco, E., & Mouchet, M., Accretion mechanisms in the Be/X-ray transient system A0535 + 26, ApJ 369, 490 (1991)

42. Muller, S., Ferrigno, C., Kuhnel, M., Schonherr, G., Becker, P.A., et al., No anti-correlation between cyclotron line energy and X-ray flux in 4U

0115+634, A&A 551, A6 (2012)

43. Munar, P., Paredes, J.M., Ribo, M., Iwasawa, K., Zabalza, V., & Casares J., Discovery of X-ray emission from the first Be/black hole system, The Astrophysical Journal Letters V 786 (2014)

44. Negueruela, I., On the Nature of Be/Xray Binaries, A&A 338, 505 (1998)

45. Negueruela, I., Smith, D. M., Reig, P., Chaty, S., & Torrejn, J. M., ESASP 604, 165 (2006)

46. Negueruela, I., & Schurch, M. P. E., A search for counterparts to massive X-ray binaries using photometric catalogues, A&A 461, 631 (2007)

47. Negueruela, I, Stellar wind accretion in high-mass X-ray binaries, arXiv:0907.2883 (2009)

48. Nelson, R., Salpeter, E., & Wassermann, I., Nonthermal Cyclotron Emission from Low-Luminosity Accretion onto Magnetic Neutron Stars, ApJ 418, 874 (1993)

49. Nesersian, A.,Study of the Optical Spectral Variability of the Be/X-ray Binary Systems (2015)

50. Nespoli, E., Reig, P., & Zezas, A., New insights into the Be/X-ray binary system MXB 0656-072, A&A 547, A103 (2012)

51. Nespoli, E., & Reig, P.,Spectral states in Be/X-ray pulsars, arXiv:1302.1693 (2013)

52. Owocki, S., Formation and Evolution of Disks around Classical Be Stars, ASP 355, 219 (2006)

53. Porter, J. & Rivinius, T., Classical Be Stars, PASP 115, 1153 (2003)

54. Priedhorsky, W. C., & Terrell, J., Long-term observations of X-ray sources - The Aquila-Serpens-Scutum region, ApJ 280, 661 (1984)

55. Reig, P., Roche, P., Discovery of Two New Persistent Be/X-ray Pulsar Systems, MNRAS 306, 100 (1999)

56. Reig, P., Negueruela, I., Papamastorakis, G., Manousakis, A., & Kougentakis, T., Identification of the Optical Counterparts of High-Mass X-ray Binaries Through Optical Photometry and Spectroscopy, A&A 440, 637 (2005)

57. Reig, P., Larionov, V., Negueruela, I., Arkharov, A.A., & Kudryavtseva, N.A., The Be/X-ray Transient 4U0115+63/V635 Cassiopeiae, A&A 462, 1081 (2007)

58. Reig, P., Rapid Spectral and Timing Variability of Be/X-ray Binaries During

Type II Outbursts, A&A 489, 725 (2008)

59. Reig, P., Be/X-ray Binaries, Astrophysics and Space Science 332, 1 (2011)

60. Rothschild, R. E., Blanco, P. R., Gruber, D. E., et al., In-Flight Performance of the High-Energy X-Ray Timing Experiment on the Rossi X-Ray Timing Explorer, ApJ 496, 538 (1998)

61. Skrutskie, M.F. , Cutri, R.M. , Stiening, R. , Weinberg, M.D. , Schneider, S. , Carpenter. , et al., The Two Micron All Sky Survey (2MASS),The Astronomical Journal 131, 1163 (2006)

62. Shakura, N. I. &Sunyaev, R. A., Black holes in binary systems. Observational appearance, A&A 24, 337 (1973)

63. Shakura, N.I., Postnov, K.A.,Kochetkova, A.Yu., Hjalmarsdotter L. , Sidoli, L. , & Paizis, A., Wind accretion: Theory and Observations, Astronomy Reports 59, 645 (2015)

64. Slettebak A. and Snow, T., Physics of Be Stars, Proceedings of IAUC 96, Cambridge University Press (1987)

65. Smith, M. A., Henrichs, H. H., and Fabregat, J., The Be Phenomenon in Early-Type Stars, IAU Colloquium 175, ASP Conference Proceedings 214 (2000)

66. Stella, L., White, N. E., & Rosner, R., Intermittent stellar wind accretion and the long-term activity of Population I binary systems containing an X-ray pulsar, ApJ 308, 669 (1986)

67. Struve, O., On the Origin of Bright Lines in Spectra of Stars of Class B, ApJ 73, 94 (1931)

68. Townsend, R. H. D., Owocki, S. P.,& Howarth, I. D. ,Be-star rotation: how close to critical?, MNRAS 350, 189 (2004)

69. Townsend, L.J., Coe, M.J., Corbet, R.H.D., & Hill, A.B., On the Orbital Parameters of Be/X-ray Binaries in the Small Magellanic Cloud, MNRAS 416, 1556 (2011)

70. Tsygankov, S. Mushtukov, A., Suleimanov, V. F., & Poutanen, J., Propeller effect in action in the ultraluminous accreting magnetar M82 X-2, MNRAS 457, 1101 (2016)

71. Waters, L.B.F.M., & van Kerkwijk, M.H., The relation between orbital and spin periods in massive X-ray binaries, A&A 223, 196 (1989)

72. Wilson, C. A., Finger, M. H., & Camero-Arranz, A., Outbursts Large and Small from EXO 2030+375, ApJ 678, 1263 (2008)

73. Woolf, N. J., Stein, W. A., & Strittmatter, P. A., Infrared emission from Be stars, A&A 9, 252 (1970)

74. http://skinakas.physics.uoc.gr

75. http://www.mporzio.astro.it/gianluca/phdthesis/node10.html

76. https://heasarc.gsfc.nasa.gov/xanadu/xspec/XspecManual.pd

77. http://xray.sai.msu.ru/~mystery/articles/review/node21.html